



LUND UNIVERSITY

Development and Evaluation of a Tomographic Technique for Volumetric Imaging of Flames

David Sanned

Thesis submitted for the degree of Master of Science

Supervised by Mattias Richter and Karl Åström

Department of Physics
Division of Combustion Physics
August 2018



© David Sanned
August 2018
Lund Reports on Combustion Physics, LRCP-214
Department of Combustion Physics
Department of Physics
Lund University
P.O. Box 118
S-221 00 Lund
Sweden

ABSTRACT

With modern day interest to continue the reduction of harmful emissions and improve the efficiency of combustion devices, the need to further improve upon accuracy and ability to describe combustive processes is of high value. Nowadays, multiple capable point (0D) and two-dimensional measurement (2D) techniques exist for flame investigation, however as combustion nearly always is a three-dimensional (3D) process some limitations do exist within many of these techniques. Therefore, the interest to find alternative ways to gather 3D volumetric information with both high temporal and spatial resolution has grown.

This work aims to develop and thereafter evaluate a tomographic technique able to acquire volumetric data from flames and thus put forward a proof of concept that can lay the foundation for future practical applications. Thus, potentially allow for volumetric flame data to be acquired from inside combustion devices with limited optical access.

The tomographic technique was built around the Additive Reconstruction Technique (ART) algorithm and was made to reconstruct both 2D and 3D synthetic flame models, the results were then studied and evaluated. Furthermore, the groundwork for an experimental setup using ten cameras was built to allow for future practical appliance of the tomographic technique in flames. This incorporated the evaluation of different cameras to find the most promising, that in turn would serve for the flame imaging. Finally, a calibration process to map each camera into the same coordinate system was performed to allow for future accurate data gathering.

The results showed that the method proposed in this work for reconstruction of 2D objects was successful, with complex objects of 200-by-200 pixel resolution being reconstructed using ten projection views. Likewise, the modifications made upon the 2D reconstruction, to allow for reconstruction of 3D objects using 2D projections, proved successful in this work. The results show that the interior intensity structure and outer shape was retained in the reconstruction of a 3D synthetic flame model with only minor aberrations present.

In the building of the experimental setup, ten acA1920-40gm-Basler-ace cameras were employed. The model was chosen due to possessing superior signal to noise ratio (SNR) performance than other evaluated models together with a higher resolution that could come of use in future work. The calibration method applied was evaluated to be successful with an individual mean reprojection error of around 0.5 pixels for every camera.

ACKNOWLEDGMENTS

I wish to thank my main supervisor Professor Mattias Richter of Combustion Physics at Lund University for giving me freedom and trust in this work, as well as always being available for discussion.

I also want to thank my co-supervisor Professor Karl Åström of Mathematics at Lund University for guidance and support when I encountered problems.

Finally, I wish to thank my family for their love, understanding and endless support.

CONTENTS

ABSTRACT

ACKNOWLEDGMENTS

INTRODUCTION.....	1
THEROETICAL BACKGROUND	3
Computer Tomography.....	3
Projections and Object space	4
3D Object Space and Projections.....	6
Ill-posed problem	7
Algebraic Reconstruction Technique (ART)	8
Camera Matrixes.....	9
PRACTICAL WORK	11
Camera selection.....	11
Signal to noise ratio	12
Optical Resolution	15
2D Model Reconstruction.....	17
3D Model Reconstruction.....	19
Space Carving	21
Tomography	22
EXPERIMENTAL SETUP	23
Camera Calibration	24
RESULT AND DISCUSSION.....	26
2D Model Reconstruction.....	26
3D Model Reconstruction.....	29
Space Carving	29
Tomography	30
Experimental Results.....	32
CONCLUSION AND OUTLOOK	35
REFERENCES.....	36

INTRODUCTION

There, is large interest for continued reduction of harmful emissions emitted from different combustion processes and the increase of the efficiency of such processes. To enable such improvements of combustion devices and to further work towards reduction of pollutants, laser-based combustion diagnostics is an important tool. It enables information gathering about important combustion characteristics due to its many non-intrusive methods.

It has long been of high value to study different kinds of flames and gaseous combustion flows using techniques such as two-dimensional (2D) Laser induced Fluorescence (LIF) and chemiluminescence measurements to gain access to information regarding species concentration, temperature, pressure, velocity and density at different flow field points [1-3]. Furthermore, other characteristics such as reaction zone studies, mixture fraction measurements and flame topography continue to be of equal interest of study [3].

However, most of these techniques are based around point (0D) or 2D measurements and thus there is a need to find a path towards full three-dimensional (3D) combustion measurements because combustion nearly always is a 3D process and often turbulent. 3D in situ measurements with high temporal and spatial resolution could give valuable information about combustion processes which normally would be hard to access. The results could potentially lead to computer modeling improvements or be applied to enable physical enhancement in combustion devices for example injector port or flame holder optimization [4, 5].

Many modern 2D-techniques enables 3D-visualization of the measurement by merging data from multiple 2D-layer measurement as done in Planar laser induced fluorescence (PLIF) where the laser sheet is scanned through the probe volume and later reconstructed into a 3D-model. However, even if technical advancements have improved the techniques, enabling high repetition rate and spatial resolution of around 1 mm in some cases, there exist limitations which are hard to overcome, such as achieving sufficiently high resolution for all applications. Therefore, the desire for alternative ways to achieve volumetric information from LIF and flame diagnostics in general with even higher temporal and spatial resolution has been of high interest over a long time [3, 6].

Due to inherent properties of flames such as transparency and emission of volumetric signals it is possible to perform tomographic reconstruction of flames. Where the volumetric signal could for example come from flame-luminescence, chemiluminescence or induced volumetric LIF-based measurements. The tomographic technique revolves around capturing the flames volumetric signal simultaneously by detectors at different viewing locations around the probe volume. The projection data gathered this way is then used in the tomographic reconstruction to produce a full 3D-model of the flame. When used with LIF, this method has previously been called Volumetric laser induced fluorescence (VLIF) or Computer Tomography of Chemiluminescence (CTC) for chemiluminescence measurements [3, 4, 7-9].

One of the advantages with using 3D-reconstruction from multiple views to produce the volumetric data is the possibility to achieve high temporal and spatial resolution as all data is gathered simultaneously, which previously has been hard to achieve [10]. Furthermore, when it comes to turbulent and unsteady flames the use of tomography reconstruction can possibly aid in the search for turbulent characteristics which are tied to the 3D properties of flames [4].

This work aims to provide a proof of concept for enabling tomographic measurements of flames and thus the reconstruction of 3D-data from multiple 2D-images by development of a computer code. The iterative computational method that will be utilized to perform the reconstruction is the Additive Reconstruction Technique (ART) algorithm. ART was chosen due to its applicability in the reconstruction problem, the generally fast solution convergence speed and the ability to incorporate a priori knowledge for future improvements to the technique. The algorithm will be applied on 2D- and 3D-model objects to evaluate potential in being utilized in tomographic reconstruction applications. Furthermore, a space-carving technique will likewise be applied in the 3D case to allow for further evaluation.

Moreover, the ground work for a laboratory setup, able to perform flame tomography studies was to be laid out to enable future practical application of the technique. This involved the selection of suitable machine vision cameras to enable the method to be utilized in applications with restricted physical space and optical access. Each of the cameras are tested for their individual signal to noise ratio (SNR) as well as their optical resolution when applied in this specific application. Finally, a camera calibration process that maps each individual camera to the same 3D-coordinate system will also be implemented to allow for the gathering of camera data.

THEROETICAL BACKGROUND

Tomography has been widely used since the 1970s in various fields such as seismology, industrial quality control and medicine, where imaging techniques such as Positron Emission Tomography (PET) and X-ray Computed Tomography have been leading the way.

Computer Tomography is based upon the measurements of many probe lines, referred to as a line integral, which travel through the object of study. Thereafter a reconstruction of the examined object can be made from the gathered projection data given by these integrals. The line measurements can be achieved in different ways depending on the nature of the experiment, measurements have been made using electron microscopes to enable reconstruction of molecular structures and data gathered from medical x-ray measurements have been used to reconstruct tissue images useful for medical evaluation. Other techniques based around measuring magnetic resonance, radioisotopes, different types of beam attenuation or optical phase differences are also viable sources of reconstruction data [11, 12].

Although mostly used to produce 2D distribution images, this technique can be expanded to provide 3D imaging data that is accurate and possibly non-intrusive depending on the measuring technique used. However, tomography requires the object of study to be transparent or sufficiently thin so that data can be collected throughout the object volume to enable the reconstruction in full three dimensions [5, 13].

Non-sooty flames are in general transparent for visible light and we can thus use the tomography approach to measure different quantity fields such as species concentration, temperature and density that are all integrated over a line of sight path. Reconstruction from flame luminosity alone should be possible as long as the flame has no soot, however effects such as self-absorption which possibly could affect the results needs to be considered [5].

Computer Tomography

The mathematical method of performing Computer Tomography is based upon the solving of an inverse problem. In practice this is done by representing the continuous object space measured as a discrete scalar field which in turn can be estimated by evaluating distinct integral measurements which spans through the object space and are acquired at known geometrical angles and positions. Basically, the object is reconstructed using its geometrical projections acquired at various angles in the object space.

Nonetheless, some limitations to this technique exist due to the object space being estimated as a discrete scalar field and thus will be different from the true continuous field. However, these errors will be a function of the resolution and thus will decrease as the resolution of the reconstruction increases. The resolution is in turn heavily connected to the number of projections of the object that is available, a higher number of projections will enable a reconstruction of higher resolution [12, 13].

Projections and Object space

To enable a good understanding of the reconstruction method it is crucial that the terms projection and object space are well defined as they are at the core of the tomography technique. The object space defines the space (volume) which the object in world coordinates inhabits, basically the space measured. The term projection will here refer to a line integral that span through the object space, when multiple similar integrals are evaluated at a specific observation angle with reference to the object space they will together create a projection view q . For the 2D-case a schematic illustration is shown in Figure 1 where two projections at different angles are taken of an object space containing two transparent cylindrical objects.

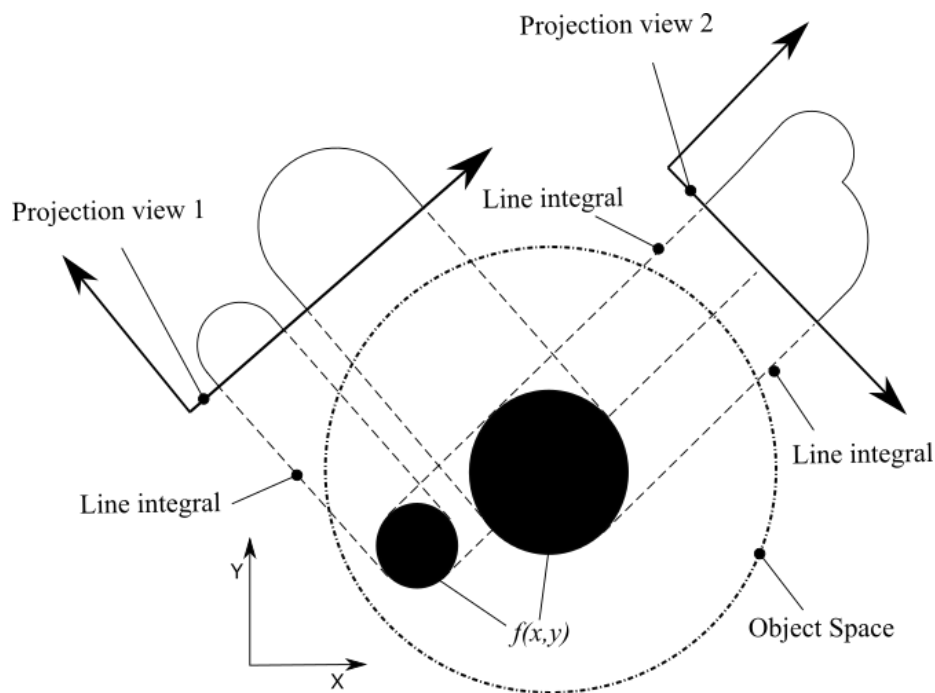


Figure 1 Illustration of two projections at different views separated by an angle of two cylinder objects with different size. The cylinder objects lie within the object space and are represented by the function $f(x,y)$.

It can be seen in Figure 1 that the integrals constructing each respective projection view are visualized as parallel lines which in reality might not always be the case due to effects such as diffraction. Nonetheless, in such cases it is possible to incorporate a change of the projection geometry to account for variations or to enable diffractive energy sources such as ultrasound or microwaves to be used to produce the projections [12].

From this concept it is then possible to define a projection operator which will return the value of a single line integral taken through the continuous object space at a specific projection angle as

$$b_{qp} = \int f(x, y) dA, \quad (\text{Equation 1})$$

where b_{qp} is the integral value of projection p on the view q and $f(x, y)$ is the function that describes the object within the object space.

However, in this work an iterative method will be used to perform the reconstruction and thus it is of interest to discretize the continuous object space into a scalar field consisting of pixels. If the object space pixels then are vectorized and numbered by the single index i one can redefine the projection operator from Eq. (1) as a summation of the scalars lying on each linear projection path as

$$b_{qp} = \sum_{i=1}^N Z_{qpi} f_i, \quad (\text{Equation 2})$$

where Z_{qpi} is the contribution of the object space pixel i to the projection p on the view q , b_{qp} is the final value of the projection qp when summed over each object space pixel i and f_i denotes the constant value of the object $f(x, y)$ within one object space pixel i .

There are multiple ways to define the contribution Z_{qpi} but the method used depends on the type of projections utilized. Further on in this work every object pixel i will be divided into smaller subpixels which in turn will be projected to find how much of each object space pixel i contributes to each projection qp . Different but similar ways have been used in works of others to define the contribution, for example one could look at the length of the intersection path of a line integral and each object space pixel [12-14].

The projection operator Eq. (2) is illustrated in Figure 2 where a projection qp is taken across an object space discretized into pixels. Each intersection between the projection and the pixels gives the individual pixel contribution Z_{qpi} to the full projection line qp .

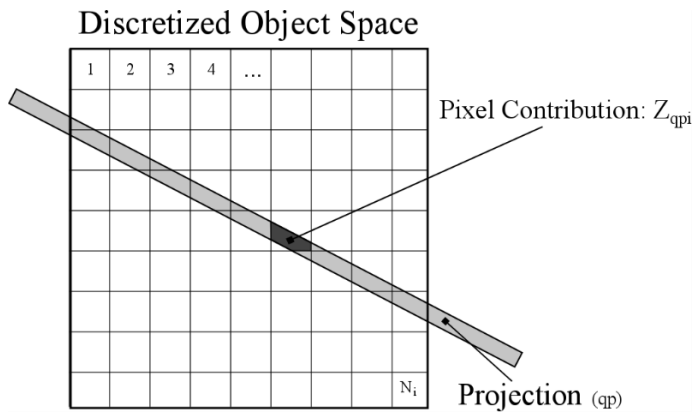


Figure 2 Discretized object space made up of N_i pixels. The contribution of a pixel Z_{qpi} to the full projection qp is the intersection of the pixel and the projection line.

Discretizing the object space and utilizing the projection operator from Eq. (2) makes it possible to express all projections for every view as a system of linear equations with the form $Ax = b$. The A matrix expressed in Eq. (3) is generally referred to as the projection matrix as it contains the information to map the projections of object space pixels to their full projection line qp . Each column of the A matrix represents a single object space pixel, thus each row of A corresponds to the contribution from all object space pixels to a full projection line qp throughout the object space. The values Z_{qpi} in the matrix will be the weight of contribution from that respective object pixel to the full projection line. However, this matrix will generally be very large and because a single object space pixel usually only contributes to a few full projection lines this matrix will also be sparse [11, 12]. The b column-vector in the equation system $Ax = b$ is the projection data gathered and the column containing the f_N values is the solution vector x , namely the vector containing the values for the object space pixels [7]. If we define M as the total number of projections p from all different views q , the full linear equation system $Ax = b$ can be expressed as

$$\begin{pmatrix} b_1 \\ b_2 \\ b_3 \\ \vdots \\ b_M \end{pmatrix} = \begin{pmatrix} Z_{11} & Z_{12} & Z_{13} & \cdots & Z_{1N} \\ Z_{21} & Z_{22} & Z_{23} & \cdots & Z_{2N} \\ Z_{31} & Z_{32} & Z_{33} & \cdots & Z_{3N} \\ \vdots & \vdots & \vdots & \ddots & \vdots \\ Z_{M1} & Z_{M2} & Z_{M3} & \cdots & Z_{MN} \end{pmatrix} \begin{pmatrix} f_1 \\ f_2 \\ f_3 \\ \vdots \\ f_N \end{pmatrix} \quad M = q \cdot p \quad (\text{Equation 3})$$

where the left-hand column-vector b contains the all measured projection values, the middle matrix is the projection matrix A consisting of the contribution weights Z_{qpi} for each object space pixel i to the full projection line p on view q . The right-hand column-vector containing the f_N values is the solution vector x and the value M is the total number of projections.

3D Object Space and Projections

The object space is now in 3D as illustrated in Figure 3. Hence it can be discretized into a set of N_i volumetric voxels with individual indices i which differ from the previous case where the 2D object space was discretized into pixels. Furthermore, a view q is now a set of 2D projections and can be thought of as a single camera image. In the 2D case the notation p represented a single projection line originating from a view q . However, in this 3D case each view q is composed of a set of 2D pixels p with indices n, m and therefore each pixel p now represents a 2D projection onto a view q . Two different coordinate systems are present, the object space coordinates x, y, z and the view coordinates X, Y, Z where notably the Z -axis points along the projection direction.

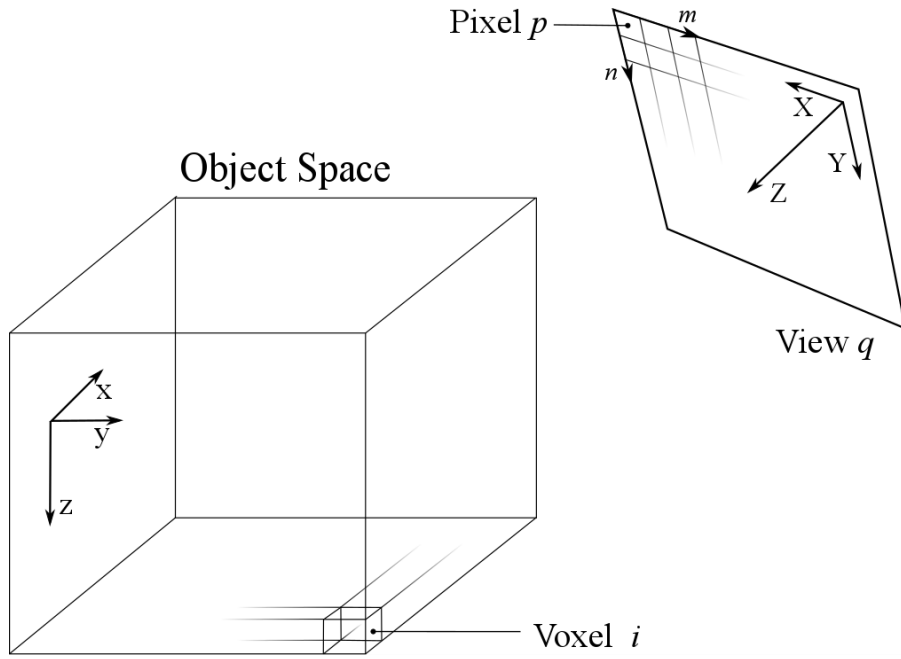


Figure 3 A 3D discretized object space made up of N_i voxels with index i . A view q is a 2D image composed of single pixels p with indices n and m . The object space coordinates are x, y, z and X, Y, Z the view coordinates.

In the same fashion as for the 2D case a projection matrix A can be built for the 3D case and a linear equation system of the form $Ax = b$ can similarly be formed as shown earlier in Eq. (3). The difference is that b_{qp} now is a measured 2D pixel projection and Z_{qpi} now will be the weight contribution from the single 3D voxel i to the projection p on view q .

Ill-posed problem

However, one inherent difficulty with performing tomography on objects using projections to build an equation system this way, is that generally the problem will prove to be ill-posed. Normally having an ill-posed problems makes it highly likely that the projection matrix A proves to be non-invertible, resulting in the inability to solve the system $Ax = b$ by computing the inverse A^{-1} [11, 15, 16].

There are typically two different ways that causes a tomographic problem to be ill-posed. The first one is matrix rank-deficiency, in this case the number of variables is greater than the number of equations in the system thus enabling an infinite number of solutions [17]. Secondly the equation system can be overdetermined, this means that the number of variables, which are given by the discretization of the continuous problem, is less than the number of available equations given by the projections resulting in the system having no solution. Sometimes, one can overcome these problems by looking for approximate solutions or applying constraints to the solution of the problem. These constraints can take the form of minimum or maximum value limitations, spatial restrictions or other applied regularization methods [18].

Algebraic Reconstruction Technique (ART)

ART is a series expansion method that can be used to solve linear equation systems of the form $Ax = b$. The technique is based upon the Kaczmarz projection method [13, 19] and works by estimating the solution vector x given a camera image vector b that contains the measured projection values and the $m \times n$ projection matrix A . The technique is sometimes referred to as a row-action method because it advances by performing calculations on one row of the A matrix at a time and consecutively adding the results from each row to the solution vector x [11-13].

The iteration routine of ART is shown in Eq. (4), the method advances by computing the difference between value of the i -th row of the vector b and the inner product of the i -th row of the A matrix a_i and the current iteration's k solution vector x_i^k . The result is scaled by the norm of the row a_i then multiplied with that same row transposed into a column-vector and finally weighted with a relaxation parameter λ_k . This routine is done for all rows a_i in A and consecutively added to the solution vector x , generally a reasonable estimation of the solution can be reached with as few as ten iterations however more iterations tend to further improve the result [11, 16].

$$x_i^{(k+1)} = x_i^k + \lambda_k \frac{b_i - \langle a_i, x_i^k \rangle}{\|a_i\|^2} a_i^T \quad i = k \bmod (m + 1) , \quad (\text{Equation 4})$$

where k is the number of iterations, m the number of rows in matrix A , x_i is the i -th row of the estimated solution vector, b_i is the i -th of the measurement vector b , a_i is the i -th row of A and λ_k is the specified relaxation parameter used for all iterations.

The relaxation parameter enables the method to be tuned towards better convergence and to lower the amount of noise in the reconstruction. However, the optimal relaxation value is difficult to determine as it depends on various factors such as noise in the projections [11]. The relaxation parameter was in this work set to constant but different values for the 2D and 3D reconstruction cases to enable better convergence and produce acceptable results. Nevertheless, improving the choice of this parameter could thus lead to even better results. ART also requires an initial guess of the solution vector x and because the algorithm has been shown to be insensitive to changes of initial vector [20], the zero-vector was used throughout this work.

Camera Matrixes

In the field of computer vision the mathematical representation of a camera's spatial position and physical characteristics such as focal length and principal point is often made using three different matrixes. These matrix representations are based on the pinhole camera model and use two different coordinate systems, world coordinates and camera coordinates (Figure 4). The world coordinates refer to the coordinate system in which the camera and the studied objects are located. The camera coordinates on the other hand refer to the coordinates of the camera image plane and thus can normally be understood as pixel coordinates. The pinhole camera is a commonly used camera model in computer vision, not only because of its simplicity but also its applicability. The model cannot handle all possible distortions but for high-quality cameras many of those effects can be neglected and the model performs satisfactorily [17, 21].

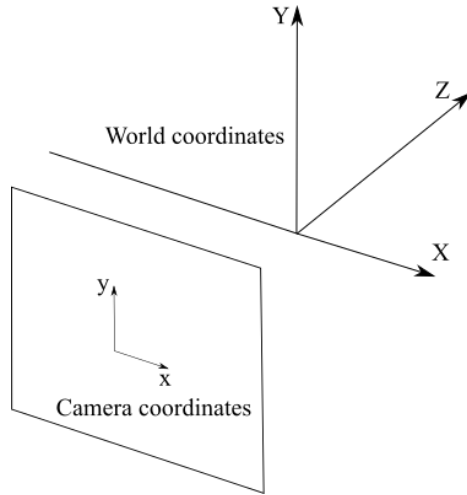


Figure 4 3D world coordinate and 2D camera coordinate system.

First, we have the extrinsic matrix which describes the camera's location in the world coordinate system. The extrinsic matrix is a 3-by-4 rigid transformation matrix, shown in Eq. (5), that is composed of a 3-by-3 rotation matrix R making up the first three columns describing the camera rotation and a translation column-vector t as the fourth matrix column [17].

$$\text{Extrinsic Matrix } [R; t]: \begin{bmatrix} r_{1,1} & r_{1,2} & r_{1,3} & t_1 \\ r_{2,1} & r_{2,2} & r_{2,3} & t_2 \\ r_{3,1} & r_{3,2} & r_{3,3} & t_3 \end{bmatrix}, \quad (\text{Equation 5})$$

where $r_{n,m}$ are the rotation matrix elements and t_n are the elements of the translation column-vector.

Secondly, we have the intrinsic matrix, shown in Eq. (6). The matrix is a 3-by-3 that contains the internal information of the camera such as the focal length, the point where the optical axis of the system intersects with the image plane named principal point and the skew between the x and y axis of the image [17].

$$\text{Intrinsic Matrix } [K]: \begin{bmatrix} f_x & s & c_x \\ 0 & f_y & c_y \\ 0 & 0 & 1 \end{bmatrix}, \quad f_x = F \cdot p_x \text{ and } f_y = F \cdot p_y, \quad (\text{Equation 6})$$

where F is the camera focal length in world-units (mm) and $[p_x, p_y]$ are the respective number of pixels per world unit. The values $[c_x, c_y]$ are the location of the principal point in pixels. The

skew between the x- and y-axis is given by the parameter s and will be equal to 0 if the two axes are perpendicular to each other.

The third and final matrix is the so called camera matrix or projection matrix and is computed from the multiplication of the intrinsic matrix with the extrinsic matrix [17] as follows

$$\text{Camera Matrix } [P] = [K] \times [R; t], \quad (\text{Equation 7})$$

where $[K]$ is the intrinsic matrix, $[R; t]$ the extrinsic matrix and $[P]$ the resulting camera matrix.

The resulting 3-by-4 camera matrix can be used to transform three-dimensional world-coordinates into two-dimensional camera image coordinates, when both are expressed in homogeneous coordinates as

$$w \cdot [x \ y \ 1] = [P] \times [X \ Y \ Z \ 1], \quad (\text{Equation 8})$$

where $[P]$ is the camera matrix, $[X \ Y \ Z \ 1]$ are the world point coordinates, $[x \ y \ 1]$ is the projected image point coordinates and w is the scaling factor [17].

Sometimes resizing an image of an object in post-production can be of interest to reduce the data size when high resolution is not needed, in other words simulating a reduction of the camera-sensor resolution. However, this requires a modification of the camera projection matrix $[P]$ to prevent the image-coordinates of any imaged object ending up on the wrong pixel-coordinates on the camera sensor. This is done by applying a transform matrix $[T]$ to the intrinsic matrix $[K]$ that scales the intrinsic matrix with a factor of 2^n as shown in Eq. (9) and thereafter computing the now modified $[P]$.

$$[T] = \begin{bmatrix} 2^n & 0 & 2^{n-1} - 0.5 \\ 0 & 2^n & 2^{n-1} - 0.5 \\ 0 & 0 & 1 \end{bmatrix}, \quad [T] \times [K] = [K_{scaled}], \quad (\text{Equation 9})$$

where $[T]$ is the transformation matrix for scaling the intrinsic matrix $[K]$ with a factor of 2^n and $[K_{scaled}]$ is the scaled intrinsic matrix. The skew s is here assumed to be zero.

The subtraction of 0.5 from the pixel coordinate in Eq. (9) correctly shifts the pixel index according to the way image pixels are indexed. For instance, the center of the $[0,0]$ pixel is not located at the coordinate $[0,0]$ but instead at $[0,5 \ 0,5]$ [17].

PRACTICAL WORK

Camera selection

The tomographic technique requires multiple views of the measured object and those can be achieved simultaneously by using multiple cameras. However, when building a tomographic setup for in situ measurements in a combustion device such as an engine the indicate design must be considered when selecting cameras. Since the optical access ports of many combustion devices generally are quite small the size of the utilized cameras must be sufficiently small. Therefore, a wide search was performed to find cameras that were sufficiently small while still processing resolution around one up two megapixels to allow for good image reconstructions. Furthermore, as multiple cameras are generally needed in these setups and the economic aspect was also considered and non-expensive cameras with the potential to fulfill the requirements were prioritized in the search.

Four small machine vision cameras were eventually put forward from the wide search as candidates for use in the laboratory setup. They all fulfilled the criterions of size and resolution while still being an economical choice. Additionally, these cameras also possessed relatively short exposure times which is critical when it comes to reduce the flame movement within one frame and achieve images for reconstruction. The selected cameras are listed below in Table 1 with their respective manufacturer information.

Table 1 List of the selected camera candidates showing their respective sensor specifications, frame rate and quantum efficiency as specified by the manufacturer. The quantum efficiency shown was measured in compliance with the EMVA (European Machine Vision Association) 1288 standard [22, 23].

Model	Sensor Type	Resolution (Pixels ²)	Pixel Size (µm)	Sensor Size (mm)	Frame rate (Hz)	Quantum efficiency (EMVA)
acA1300-60gm - Basler ace	e2v EV76C560 CMOS	1282 × 1026	5.3 × 5.3	6.8 × 5.4	60	54.0 %
acA1300-30gm - Basler ace	SONY ICX445AL CCD	1296 × 966	3.75 × 3.75	4.9 × 3.6	30	57.0%
acA640-300gm - Basler ace	PYTHON NOIP1SE0300A CMOS	640 × 480	4.8 × 4.8	3.1 × 2.3	376	54.0 %
acA1920-40gm - Basler ace	SONY IMX249LLJ-C CMOS	1936 × 1216	5.86 × 5.86	13.3 Diagonal	42	70.0 %

The four selected cameras were intentionally chosen to possess different sensor sizes, sensor types and resolutions to enable a small overview of different camera types, such that the most suited one for this work could be selected. However, this poses some difficulty when it

comes to performing a justified comparison of the cameras as they are made inherently different. Therefore, they were evaluated by comparing their overall qualities mentioned above such as exposure time, quantum efficacy and frames per second (FPS). Two qualities which are necessary to enable a good and accurate reconstruction in the final experimental setup were experimentally evaluated, namely the signal to noise ratio (SNR) and the optical resolution.

Signal to noise ratio

The Signal to noise ratio (SNR) of each camera was compared by first imaging a premixed flame with all cameras at varying exposure times. These measurements were performed in a setup (Figure 5) that was made both structural and optically similar to the final tomographic setup to ensure usability of the test results. The setup consisted of a Bunsen burner producing a premixed methane flame at near stoichiometry, achieved using mass flow controllers. The flame luminosity was then imaged in turn by each respective camera at the same placement. The objective used for the imaging was a Nikon NIKKOR-O lens with a focal length of 35mm and an aperture number of $f/2$, the aperture of the objective was kept fully opened.

The distance of 680 mm between the camera lens and the center of the burner was chosen so that the whole premixed methane flame could be covered by the smallest sensor's field of view, present on the acA640-300gm model, thus enabling all cameras to fully cover the whole flame.

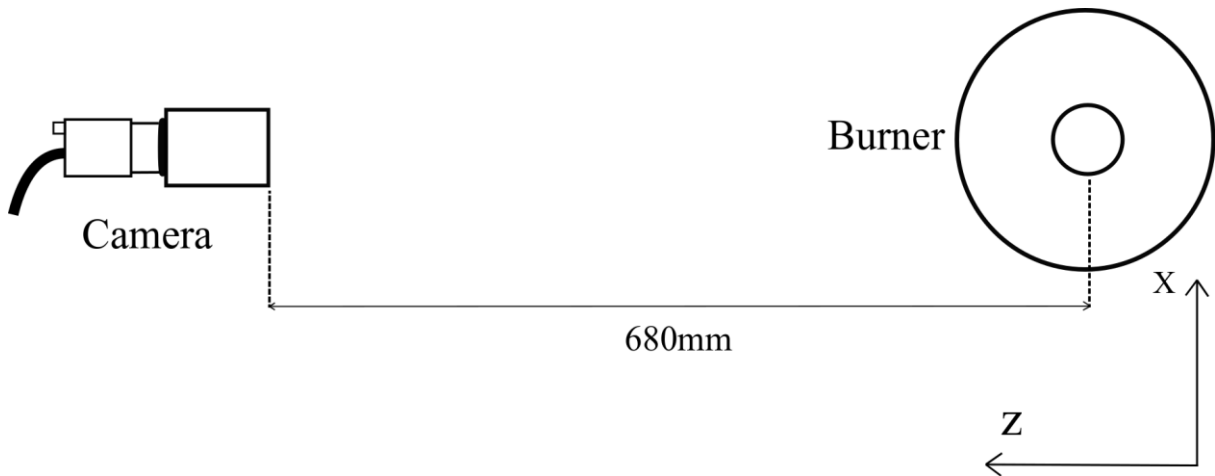


Figure 5 Schematic overview of the experimental setup used during the camera evaluation. The lens used was a 35mm focal length Nikon with an aperture number of $f/2$. The distance between the camera lens and the burner center was 680mm.

The SNR can generally be defined as the ratio between the signal power and the power of the Gaussian distributed noise within a measurement [24], as follows

$$SNR = \frac{P_S}{P_N} , \quad (\text{Equation 10})$$

where P_S is the signal power and P_N is the noise power.

The SNR of each camera was determined by comparing the standard deviation of non-background areas with homogeneous signal intensities to averaged peak signals within images taken by each individual camera of the methane flame [25]. The selection of the intensity regions is illustrated in Figure 6 displaying where the signals were acquired, the homogeneous signal area is represented by the blue square and the later averaged peak signals are taken from the flame front indicated by the green arrows.

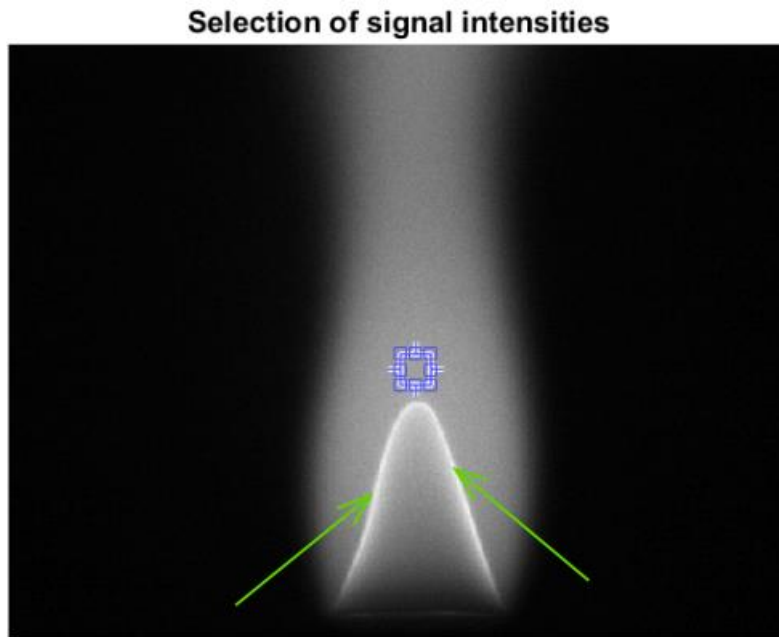


Figure 6 Selection of intensity regions for SNR evaluation. The non-background homogeneous signals are indicated by the blue square region, and the non-saturated high intensity signals were taken from the flame front, indicated by the green arrows.

For each camera several images were captured with different exposure times, this was done to enable a comparison of the cameras SNR levels over a range of exposure times, spanning from 5000 μs down to 80 μs shown in Figure 7.

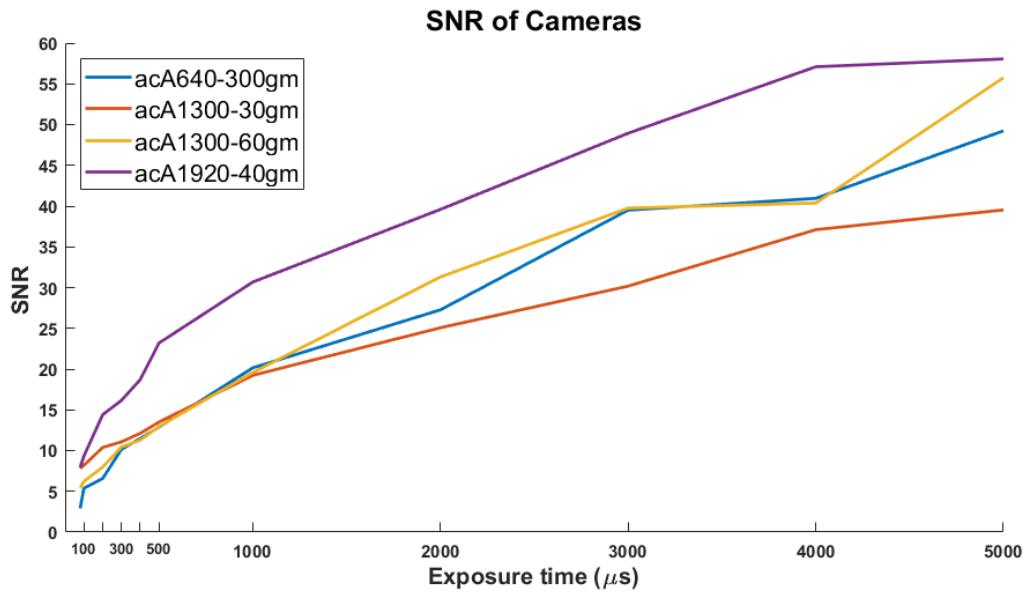


Figure 7 SNR values of all four cameras at different exposure times. Due to the experimental requirements of a low exposure time the sampling rate was increased below 500 μs to give a better overview of the lower regions.

The results in Figure 7, shows that all four cameras as expected display SNR values which are low at the shorter and more applicable exposure times at around 100 μs . However, the acA1920-40gm camera and acA1300-30gm still had almost double the SNR compared to the other two models at those short exposure times.

Furthermore, at increasing exposure times the acA1920-40gm was the camera model which showed best performance over the tested exposure time region with the two models acA1300-60gm and acA640-300gm following close behind. The model with the lowest SNR values was the acA1300-30gm, nonetheless its performance was equal to the two previously mentioned models at low exposure times of around 500 μs to 1000 μs and even proved to be superior at even lower exposure times.

The errors in this comparison are expected to be small due to the stability of the setup, however the possibility of small deviations in the distance between each of the cameras and the flame on the scale of mm's is present. However multiple measurements were performed, and the individual results compared very well to each other. Furthermore, it must be understood that in theory all four cameras should work just fine for use in the 3D tomography setup. The goal of this evaluation is to find the camera which has the best performance potential in such a setup and less about how each of the cameras compare to each other in detail.

Optical Resolution

The difference in optical resolution between the four cameras was evaluated by finding the maximum spatial frequency that each of the cameras could reproduce while using the same optics. Spatial frequency is the frequency of which a sinusoidal component of the Fourier transform of the transported image repeats itself per unit of distance, the higher frequencies will then give the sharp details. Thus the maximum spatial frequency will correspond to the maximum resolution the optical system is able to reproduce [26].

The maximum spatial frequency was determined by imaging a resolution test target (NBS 1963A) with each camera, seen in Figure 8. The target was placed at the same distance of 680mm from the objective as in the previously performed SNR evaluation. The resolution target consists of multiple different sets of five lines which have different line frequencies, this gives the possibility to determine the maximum spatial frequency (cycles/mm) that can be transported by each respective camera when coupled to the same optics [26] .

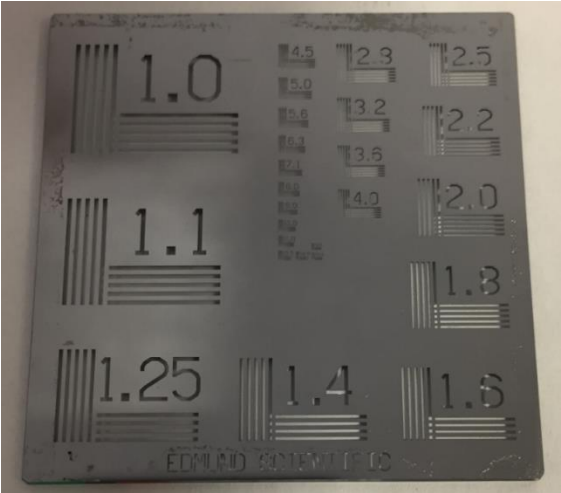


Figure 8 The NBS 1963A resolution target used to determine the highest spatial frequency each camera could resolve when using the same Nikon 35mm focal length and f/2 aperture sized objective.

The evaluation was performed by measuring pixel rows across decreasingly spaced line sets corresponding to different spatial frequencies on the resolution target image of each camera. This was done until all five peaks, corresponding to the five lines, could no longer be resolved on the crossing pixel row. The results can be seen in Figure 9 where each intensity peak represents a bright line on the target image.

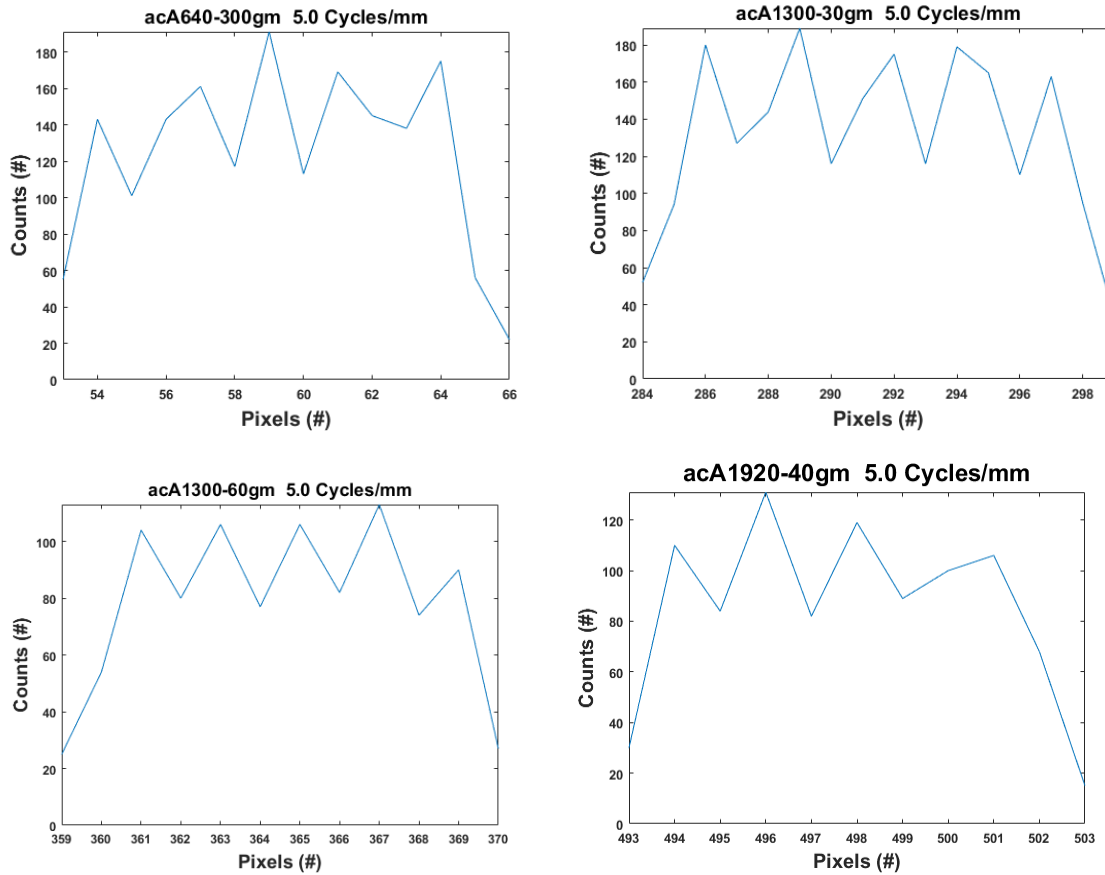


Figure 9 Resolution evaluation of the four camera models at a spatial frequency of 5.0 cycles/mm. The images show that all cameras except acA1920-40gm are able to resolve all of the five peaks in the line set.

The results in Figure 9 shows that the resolution of the system is very similar between the different camera models. However, it is observed that the acA1920-40gm was unable to resolve all five of the line peaks at a spatial frequency of 5.0 cycles/mm which would indicate a resolution limit of the system while using that camera and lens combination. It must be noted however that the comparison of resolution is not complete fair as the evaluation distance was kept constant and that the cameras pose vastly different maximum resolutions and pixel sizes. These aspects are the reason for the intensity and x-axis length being different between the cameras. Therefore, it must be said that the model acA1920-40gm should be able to resolve much higher resolutions if it was moved closer to the target. Furthermore, the resolutions achieved with all cameras are beyond what will be utilized for this tomography reconstruction due to limitations of the computational process but could be of much use in future work. It must also be taken into account that small potential errors in alignment distance between the target and objective will affect this resolution test.

Following these results, the acA1920-40gm camera model was chosen to be used in the 3D tomography setup further on in this work. Due to showing adequate results in the both the SNR and resolution evaluation. Furthermore, the higher resolution of the sensor could potentially allow for higher resolution in future 3D reconstructions where the environment and optics are different.

2D Model Reconstruction

To understand and evaluate the process of the chosen reconstruction method some simple reconstruction tests were first performed on 2D-objects composed of synthetic data. Hence, the location of the object data values was known enabling the reconstructed image to be compared to the original.

Firstly, a very simple 4-by-4 pixel object was created, seen in Figure 10, the structure of the image was chosen to have a zero-intensity region in the middle to better visualize the tomographic concept.

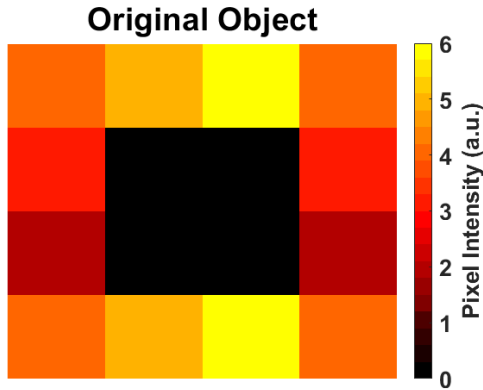


Figure 10 4-by-4 pixel 2D-object with an intensity range from zero up to six and constructed to have a zero-intensity region inside.

Two views at a 90° angle difference, one from the right and the other from the bottom were used to reconstruct the object. Each view was created as the summation of the objects pixel intensity along the view path. The right view summed the rows of the object and the bottom view summed the columns as

$$\begin{array}{rcl}
 \text{View Right } 1 & = & I_{11} + I_{12} + I_{13} + I_{14} \\
 \text{View Right } 2 & = & I_{21} + I_{22} + I_{23} + I_{24} \\
 & \vdots & \vdots \\
 \text{View Right } 4 & = & I_{41} + I_{42} + I_{43} + I_{44} \\
 \text{View Bottom } 1 & = & I_{11} + I_{21} + I_{31} + I_{41} \\
 \text{View Bottom } 2 & = & I_{12} + I_{22} + I_{32} + I_{42} \\
 & \vdots & \vdots \\
 \text{View Bottom } 4 & = & I_{14} + I_{24} + I_{34} + I_{44}
 \end{array} , \quad \text{Equation 10}$$

where I_{ii} is the intensity of a row-column indexed object pixel. The four pixels in the right view is made from the summation of the four rows. Similarly, the pixels in the bottom view is made up from the summation of the four columns.

Having these projection views, a linear equation system can be formed as shown in Eq. (3). Due to the small size and simple nature of this system, an inbuilt Matlab function *mldivide* for solving linear systems of the form $Ax = b$ for x was used. The function *mldivide* is versatile and chooses from a variety of linear equation solvers to enable speed optimization based on symmetry and how sparse the matrixes are, the function was incorporated in the Matlab R2018a version [27]. A reconstruction was also performed using a constraint to have pixels close to each other have their values to be of similar intensity as a test to try to remedy the ill-posed equation system allowing for better solution [17, 18].

Thereafter a more advanced 8-by-8 pixel object, seen in Figure 11, was created with a zero-intensity region located in the middle and corners of the object. The structure was

intentionally made similar to the previously reconstructed 4-by-4 pixel object. Seven projections were used for this reconstruction and were recorded at angles between 0° and 160° around the object.

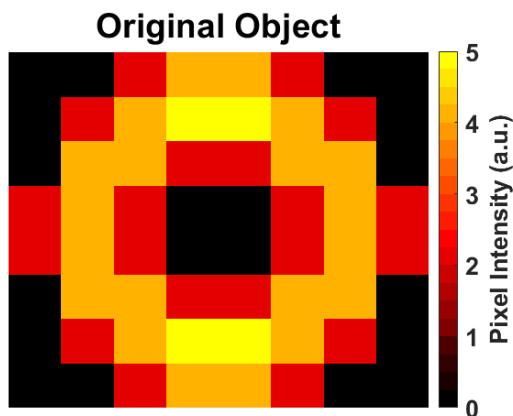


Figure 11 8-by-8pixel 2D object with an intensity range from zero up to 5 and constructed to have a zero-intensity region inside.

Due to the more complex nature of this object, the effect of adding more projection views could be evaluated. However, the projection views now needed to be acquired at multiple different angles and therefore a more advanced method to construct the projections was implemented.

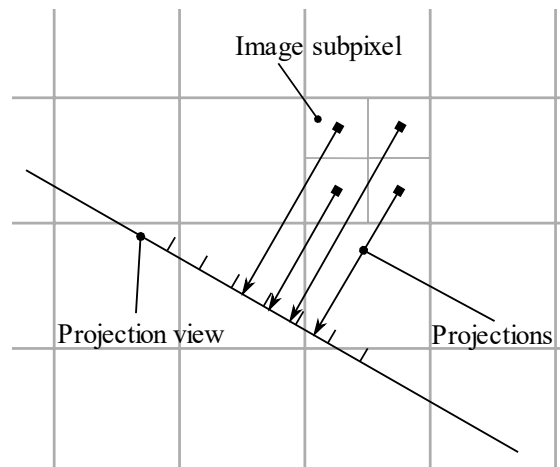


Figure 12 Projection method used to allocate each object pixels contribution onto the projection view. Each object pixel was divided into four smaller subpixels that were individually projected onto the projection view. The contribution of one subpixel was distributed evenly into the two closest projection bins to their projection location.

The method was based around dividing each pixel of the object into four smaller subpixels and thereafter projecting each subpixel onto every projection view as illustrated in Figure 12. The projection line originates from the subpixel centers and their contribution is divided proportionally between the two closest bins to the projection intersection on the projection view. If the projection line intersects exactly at the boundary between two bins the contribution of the subpixel is evenly divided into the two bins. Furthermore, if the projection line intersects in the middle of a bin that bin receives the full contribution of the sub pixel which equals one fourth of the corresponding image pixel [28, 29]. This method was implemented with help of the

Radon Matlab function [30] to achieve every object pixel's contribution to the different projection views.

In the same manner as in the reconstruction of the smaller 4-by-4 pixel object, the problem was constructed as a linear equation system. By virtue of the 8-by-8 pixel object still being small and thus giving a small projection matrix A , the problem was once again solved using the *mldivide* Matlab function R2018a [27].

The final 2D object to be reconstructed was a 200-by-200 pixel object (Figure 13) of a 2D synthesized flame utilizing the same projection method applied on the previous 8-by-8 pixel object. The number of projection views was now increased to 10 and they were recorded at angles between 0° and 160° .

To solve the now larger linear equation system and impose a constraint of only accepting non-negative solution values the ART algorithm shown in Eq. (4) was implemented using parts of the *AIR Tools II* Matlab toolbox [31]. The relaxation parameter λ_k was at the beginning set constant equal to one as it proved to give an adequate reconstruction result and the initial guess of the solution vector x was put to equal the zero-vector. To further evaluate the method, different numbers of iterations was used and the value for the relaxation parameter was eventually changed, giving a view into the effects of these variables.

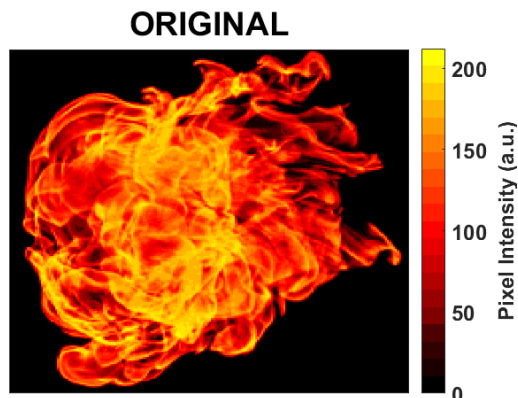


Figure 13 200-by-200 pixel 2D synthesized turbulent flame object with an intensity range from zero up to 210.

3D Model Reconstruction

To enable the transfer of the tomographic technique used in the 2D case into also working in 3D and to assess the techniques performance a 3D flame model was created. Having such a model permits the resulting reconstruction to be adequately compared to a known solution. However, before the tomography method was implemented another technique called Space Carving was performed on the flame model to evaluate the projection technique used in the tomographic reconstruction.

The 3D model of a premixed Bunsen burner flame was constructed in the open source 3D creation suite Blender [32]. The model was created to be stationary in a 3D environment where virtual cameras could be rotated 360° around the flame to enable projection images to be captured at certain angle intervals as seen in Figure 14. The flame was made to be transparent and also to emit light similar to the chemiluminescence of a Bunsen flame.

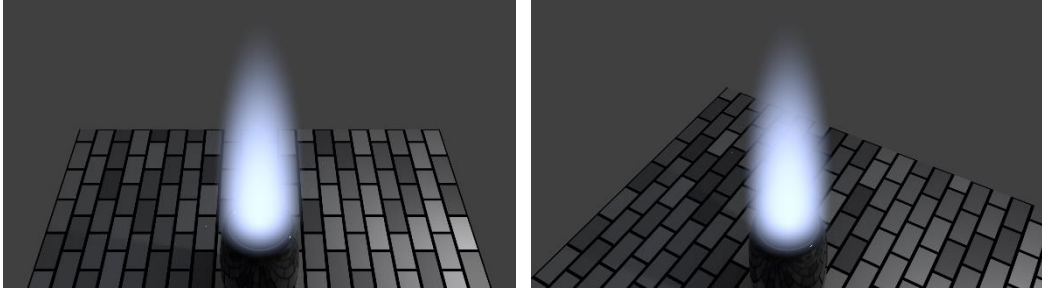


Figure 14 Images of the created static Bunsen flame model. These two images were acquired at positions located at equal distance around the flame center, separated by an angle of 150° .

For both the space carving and tomographic reconstruction eight projection images at different positions around the flame were used. They were acquired using the monochrome virtual cameras with a full resolution of 1920-by-1080pixels. Each virtual camera was placed on a plane slightly above the flame object on a circular trajectory extending 360° around the burner looking down. The eight projection images were acquired by the virtual cameras at positions of 0° , 60° , 90° , 150° , 190° , 220° , 280° and 310° around the circular trajectory, due to the elevation of the camera position plane each camera was granted a 45° downward view of the flame.

In Figure 15 a monochrome projection images of the flame model acquired by a virtual camera can be seen. Each projection image only contains the luminosity from the flame to simulate the images being acquired in a completely dark room free from interfering light.



Figure 15 Monochrome projection image of the flame acquired by a virtual camera in Blender. Only the luminosity of the flame is made to show during the data acquisition.

A python script was written to produce the intrinsic matrix $[K]$ Eq. (5) and the extrinsic matrix $[R; t]$ Eq. (6) for each virtual camera in the Blender 3D suite. The matrixes were extracted at every imaging position along the circular trajectory around the flame and thereafter each camera's projection matrix $[P]$, was calculated using Eq. (7).

Space Carving

Space carving is the technique of utilizing multiple images of an object taken at different positions to compute back the shape of the object in 3D and sometimes even the surface texture [33]. The technique is a simpler form of tomography in the sense that both techniques discretize the object-space into voxels and produce a 3D object using projections. However, in contrast to tomography where the whole interior structure is recovered only the outer shape is recovered in the space carving technique. The technique works by carving away non-object voxels by use of projection images and thus leaving the discretized space to only accommodate the 3D object [34].

Considering that only the exterior surface is of interest when using the technique, the projection images Figure 15, can be simplified into binary images to reduce data size and to simplify the carving process. This is done by giving every image pixel with any flame intensity the value of one and all the other pixels with no intensity the value of zero, the resulting binary image of the Bunsen flame is shown in Figure 16.

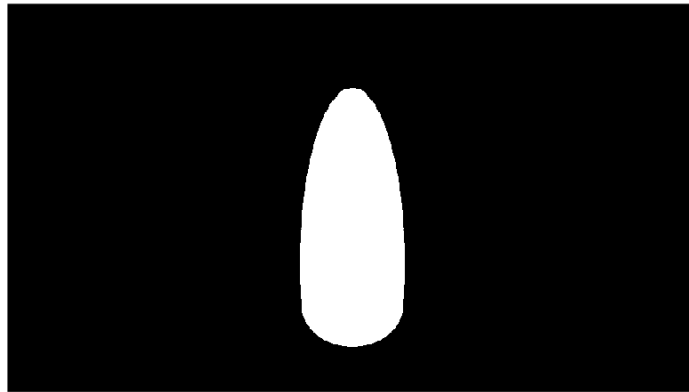


Figure 16 Projection image of the Bunsen flame turned into a binary image, all values where the intensity is not zero has been set to equal one, the rest are set to equal zero.

The object space was discretized into $160 \times 160 \times 320$ voxels and each voxel was projected onto all the eight virtual camera views using their respective 3D-world coordinate and Eq. (8). Because the projection images now were binary, every voxel projected onto an image pixel with value zero could be removed and only voxels projected onto image pixels with value one was kept. The resulting voxel space then contained the 3D outer shape of the imaged Bunsen flame.

Due to the high resolution of the projection images, the data became quite large, to save memory and speed up the process the images were scaled down to 960-by-540pixels. The image resizing was done in post-processing using bicubic interpolation which gives the output pixel a weighted average of the pixels in the closest 4-by-4 adjoining area. This was implemented using the Matlab function *Imresize* [35]. Reducing the size of the images required the intrinsic matrix $[K]$ to be modified to account for the size change. This was performed using the transformation shown in Eq. (9) with n equal to -1, yielding a scaling factor of 0.50.

Tomography

The tomographic reconstruction was performed employing the same eight virtual cameras and their respective camera matrixes used in the previous space carving technique. However, now the unmodified projection images, shown in Figure 15, were used as the data input instead of binary images.

Due to a limitation in the code that computed the camera matrixes for the virtual cameras, the resolution of the acquired images was fixed at 1920-by-1080 pixels. The images were thus later resized down to 480-by-270 pixels to reduce memory usage and to speed up the computational process, in the same way as for the space carving technique using the Matlab function *Imresize* [35]. The camera matrixes were likewise transformed to account for the change in image size using Eq. (9) with n equal to -2 to yield a scaling factor of 0.25.

The object space was discretized into 10-by-10-by-20 voxels and every voxel's 3D-world coordinate was then projected onto each of the eight camera views using Eq. (8). The low number of voxels was chosen due to an inefficiency in the way the full reconstruction algorithm stored the now very large projection matrix $[A]$, preventing the use of more voxels at this point. Thereafter, the projection matrix $[A]$ was built containing all the voxel contributions to each projection view pixel. The data column b was built by column stacking each of the projection images and consequently the linear equations system could be formed according to Eq. (3).

The equation system was solved using the ART algorithm shown in Eq. (4) which was implemented using parts of the *AIR Tools II* Matlab toolbox [31]. The minimum accepted solution value was set to zero thus preventing negative solutions and adding one constraint to the system. The zero vector was used as the initial guess for the solution vector and the relaxation parameter was set to equal 0.001, which has proven to be successful in other works applying ART for 3D tomographic reconstruction [18, 36].

EXPERIMENTAL SETUP

The purpose of building the experimental setup was to start a process to allow for the tomographic technique described in this work to eventually be made applicable experimentally. The setup was built using ten machine vision cameras of the previously selected model acA1920-40gm. The object chosen for visualization was a premixed methane flame produced by a Bunsen burner together with a mass flow controller. This kind of flame was chosen due to its potential of showcasing the tomographic technique by having a flame front that creates a shell-like intensity structure that should be possible to reconstruct.

A schematic overview of the setup is showcased in Figure 17 and an image can be seen in Figure 18. The ten machine vision cameras were arranged in an array located on the same plane on a semi-circle around the Bunsen burner to allow images to be acquired at different angles. Each camera was connected using a Cat-5e ethernet cable to a 16-port switch (EdgeSwitch ES-16-150W) with power over ethernet (PoE) capabilities to handle both data transfer and power supply.

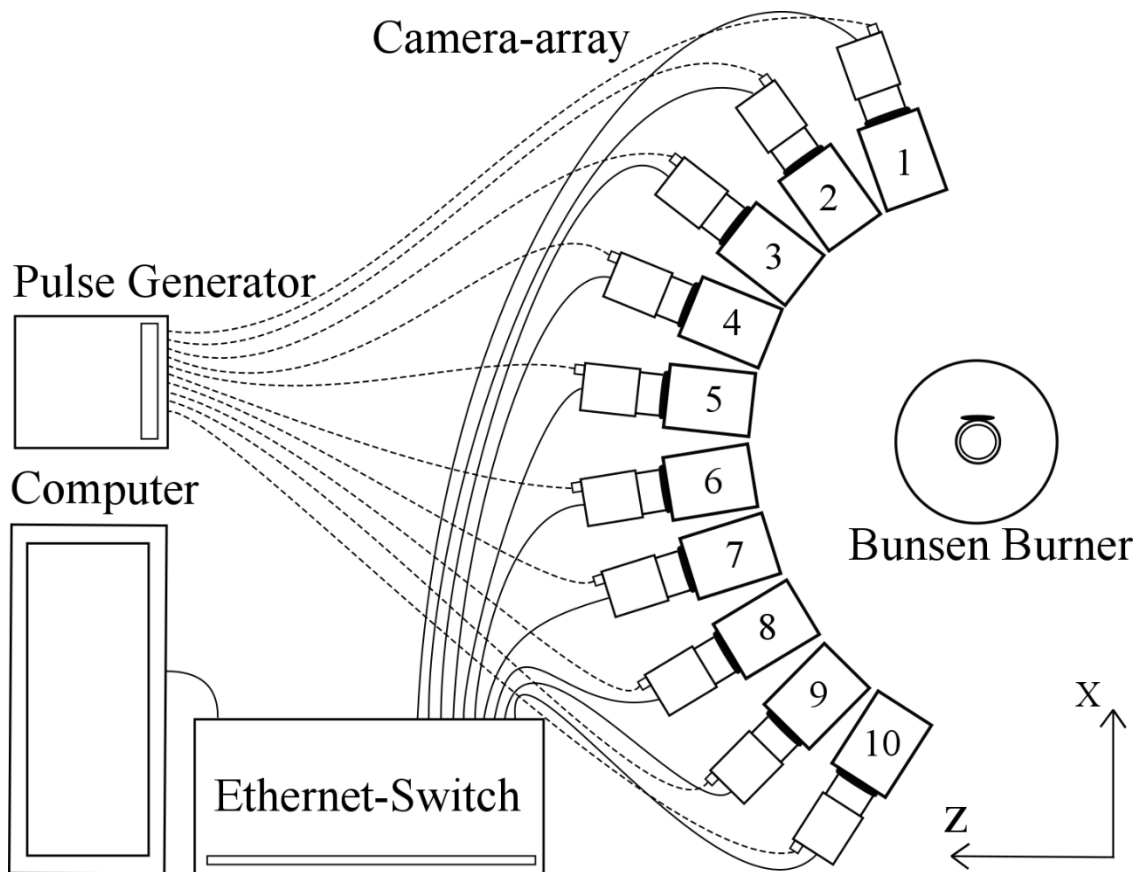


Figure 17 Schematic view of the experimental setup containing the camera-array, Bunsen burner, ethernet-switch, computer and trigger source.

The cameras general purpose I/O (GPIO) line was likewise connected to a pulse generator (9514PLUS) using Hirose (HR10A-7P-6S) cables. The generator produced a 5V pulse at command and each camera was set to acquire a single frame at the rising edge of the pulse.

Ten Nikon-AI lenses with a focal length of 28mm and a maximum aperture size of 2.8 were used for the camera array. These lenses were chosen due to their optical quality, their larger aperture size compared to other similar models allowing for collection of more signal and their low cost. The use of F-mount to C-mount adapters (Fotodiox:NikF-C-Pro) made these lenses fit on the cameras and because no size restriction was placed in the experimental setup the lenses being larger than the cameras themselves applied no hindrance.



Figure 18 Picture of the experimental setup consisting of the camera array and Bunsen burner.

The finalized setup was tested by acquiring multiple simultaneous images of the premixed Bunsen flame from all ten cameras.

Camera Calibration

The experimental implementation of tomographic reconstruction requires the spatial orientation and location of every camera used to be known with sufficient accuracy. However, performing manual measurements and acquiring sufficiently good results are quite difficult and impractical especially in setups where multiple cameras are being used. Therefore, an automatic method to register multiple camera positions and their orientation is of interest to allow for more arbitrary camera placement around the studied object.

Projected geometry is a method used in computer vision to describe imaged objects based on images acquired of that object, it also allows for the determination of camera locations together with their intrinsic parameters [37]. Therefore, a computer vision method was tried when performing the camera registration. Computer vision can utilize image feature detection to produce both the extrinsic (Eq. 5) and intrinsic (Eq. 6) camera matrixes and thus acquiring the camera matrix (Eq. 7). This process is generally called camera calibration and allows for the mapping of coordinates from the 3D object domain to the 2D images of each camera employed in the setup. Normally, these calibration techniques utilize a 2D calibration target made with specific features such as checkerboard or a board with points to allow for simpler feature detection. However, techniques exist that either use features on the actual object imaged to calibrate or use three dimensional targets such as diode structures [38-40].

In this work the camera calibration was implemented using the *camera calibrator* functions that are part of the Computer Vision System Toolbox for Matlab R2018a [41]. The calibration methods utilized in this toolbox are based on the work of Zhang [42]. Employing such an automatic method compared to manual, generally yields faster calibration times and enables the calibration to be performed more easily in complex geometric structures which is desired. This specific toolbox utilizes a calibration object in the shape of a checkerboard with

alternating black and white square boxes. The pattern has different numbers of boxes in the x and y direction to enable orientation and the normal to the checkerboard plane denotes the z direction.

The calibration process was in this work performed in three consecutive steps. Firstly, multiple simultaneous images of the calibration target were acquired by each camera in the setup. The target was moved slightly within the object volume in-between each frame such that multiple different images were acquired, one such image example is shown in Figure 19. The method recommends the use of 15 images or more which are acquired at different orientations and angles while being spread across the camera image. Therefore, approximately 90 such images were acquired for each camera to enable better results.



Figure 19 Example of a calibration image with a checkerboard target.

Thereafter, each camera was calibrated and its camera matrix and parameters were calculated. However, it should be noted that not all calibration images could be used in every camera calibration as images where all corners of the checkerboard could not be identified, due to rotation or the pattern being out of view for that specific camera, were discarded. This was done because the technique required all corners to be detectable in order to perform the calibrations. Finally, all ten cameras were spatially linked together by mapping each camera to a common calibration image where the checkerboard was placed at the flame position while being clearly visible in the images from all cameras. This enabled the extrinsic, intrinsic matrix and camera matrix to be computed and thus marked the completion of the camera calibration process.

RESULT AND DISCUSSION

2D Model Reconstruction

The goal of the tomographic reconstructions of 2D models was to demonstrate the tomographic technique and showcase some of the difficulties that apply when solving ill-posed problems. Furthermore, testing the ART algorithm on the simpler 2D case could possible allow for a smoother transition into 3D.

The results from the initial tomographic reconstruction of the 4-by-4pixel object without any restriction applied can be seen to the right in Figure 20. This unsatisfactory result showcases some of the difficulties that comes with solving ill-posed problems. The distorted reconstruction is most likely a result of the multiple solutions available to the equation system, when the problem is ill-posed, uses only two projection views and have no applied constraints. Additionally, one can notice the reconstructed image having pixels with negative intensity values, these are not physically possible but as no constraints have been applied preventing this, it becomes a computationally valid solution.

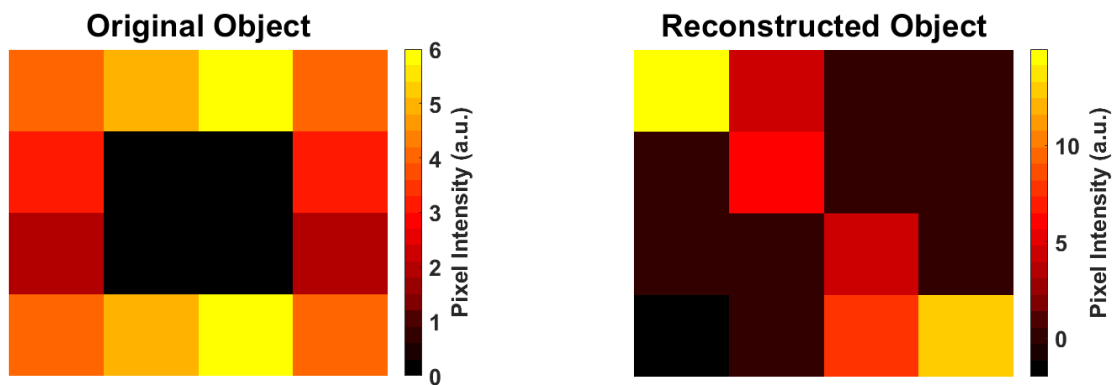


Figure 20 4-by-4 pixel object to the left and the first reconstruction to the right. The reconstruction was made using two projections orthogonal to each other and no applied constraints.

The second reconstruction had a constraint applied that forced nearby pixels to have similar intensity values and the resulting reconstruction can be seen in Figure 21. By applying the constraint, the general shape of the object could be recovered. However, such a constraint is not optimal for such a small 2D object with very large gradients, nevertheless the added constrain does slightly enhance the reconstruction towards the original shape. The existence of multiple solutions to the equation system is most likely the main cause for the result being unsatisfactory. By applying more projections and constraints into the reconstruction method the result is expected to improve further.

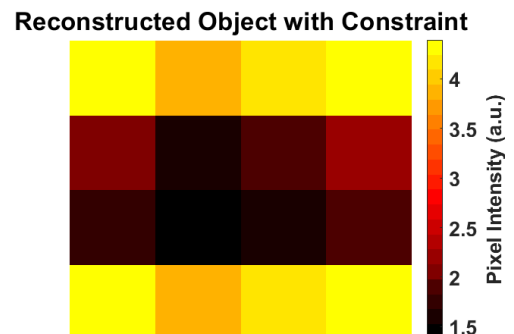


Figure 21 Second reconstruction of the 4-by-4 pixel object. The constraint of forcing nearby pixels to have similar values was applied.

The reconstruction of the 8-by-8 pixel object by the ART algorithm can be seen in Figure 22. The positive effect of using a more advanced projection method that allows the utilization of seven projection views is immediately apparent. The reconstructed object without any constraints applied on the solution vector was shown to be not so different from the original, only displaying some minor deviating features.

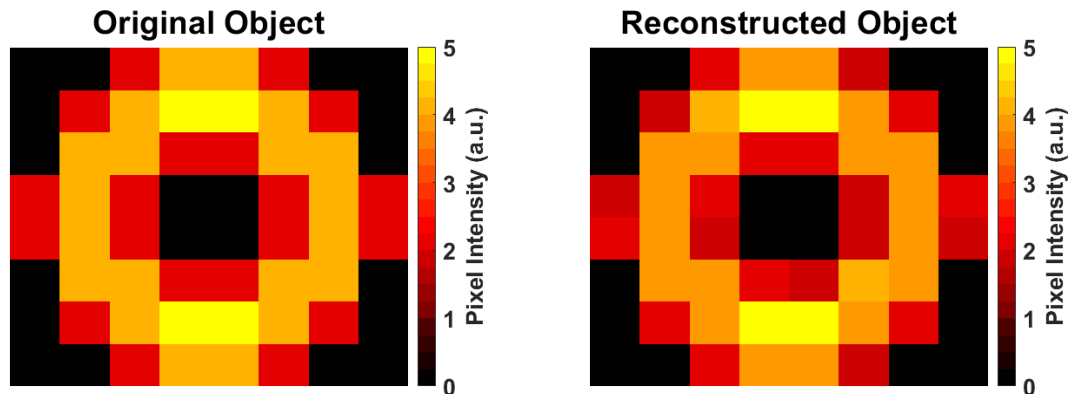


Figure 22 The 8-by-8 pixel object constructed using ART with no constraints and seven projection views to the right compared to the original object to the left.

The result (Figure 22) shows that the main features and overall structure of the object, including the zero-intensity region at the center, has been captured by the reconstruction. However, some small divergences from the original image in the form of intensity value differences can be noticed in the red and orange region surrounding the zero-intensity region in the center. However, when computing the absolute difference between the two images (Figure 23) the intensity difference is noted to be on the order of 10^{-12} thus making the result fairly respectable.

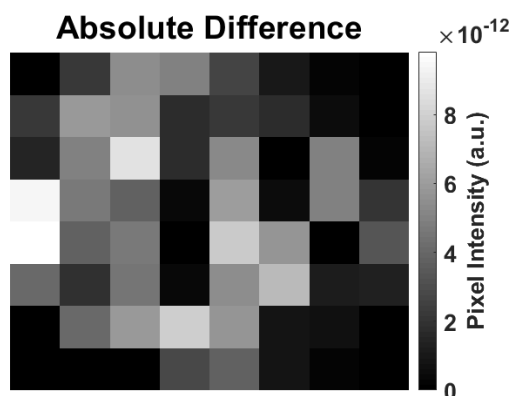


Figure 23 The absolute difference in pixel intensity between the original and reconstructed 8x8 pixel object.

The resulting reconstruction of the 200-by-200 pixel synthetic flame object using ten projection views can be seen in Figure 24. The relaxation parameter λ was set to equal one, ten iterations k were used and a constraint of accepting no solution values below zero was applied. Comparing the reconstruction to the original shows that the overall shape has been retained as well as the general locations of intensity. Important to note however are the straight lines that crosses the reconstructed image at certain angles. These image aberrations are most likely originating from the projection geometry used and perhaps by applying more projection views at different angles one can reduce their presence.

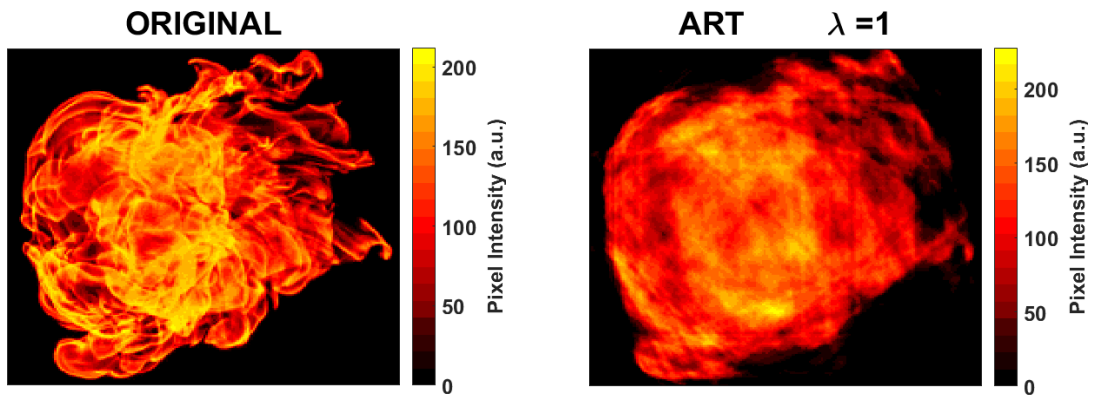


Figure 24 The 200-by-200 pixel object when reconstructed using ART to the right compared to the original object to the left. No negative solutions were allowed, ten projection views were employed together with a relaxation parameter λ of one and ten iterations k .

It is of further interest to compare the results of the initial ART reconstruction (Figure 24) with another reconstruction where the relaxation parameter and iteration number has been changed. The second reconstruction (Figure 25) used the same projection geometry, however it had a lower relaxation parameter of 0.01 and a higher iteration number of 200 than the initial reconstruction.

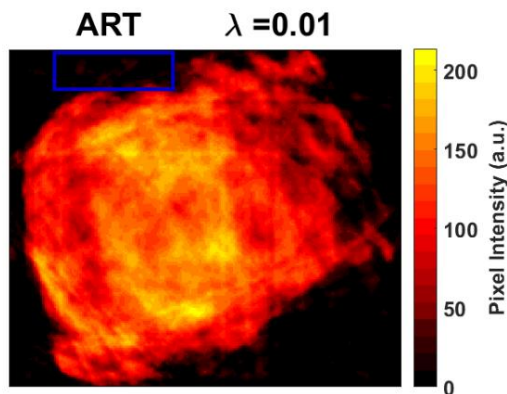


Figure 25 The 200-by-200 pixel object when reconstructed using ART. No negative solutions were allowed and ten projection views were employed together with a relaxation parameter λ of 0.01 and 200 iterations k .

Both reconstructions are similar and exhibit almost identical image aberrations which further suggests the projection geometry being the source of them. Nevertheless, some differences are present, one is the less defined shape in the second reconstruction indicated in the blue box in Figure 25, thus resulting in regions having intensity which in reality should have none.

This comparison improves the understanding of the variables used in the reconstruction and their importance when it comes to finding a solution. More importantly however, it also illustrates the difficulty of choosing the ART parameters to provide an acceptable solution.

3D Model Reconstruction

The goal of performing tomographic reconstruction of a 3D model flame was to showcase the previous 2D tomographic technique when modified to work in 3D environments and thus act as a proof of concept for the applicability of the technique in experiments. The initial space carving was performed to evaluate the projection geometry used in the 3D tomographic technique and its ability to capture the outer shape of the flame.

Space Carving

The space carving at increasing voxel resolution (Figure 26) was performed using eight camera views originating from virtual cameras surrounding the model flame in the Blender suite. The resolution of the projection images used was 960-by-540 pixels and the voxel space which was projected and thereafter carved had a size increasing from 20x20x40 up to 160x160x320 of cubic voxels.

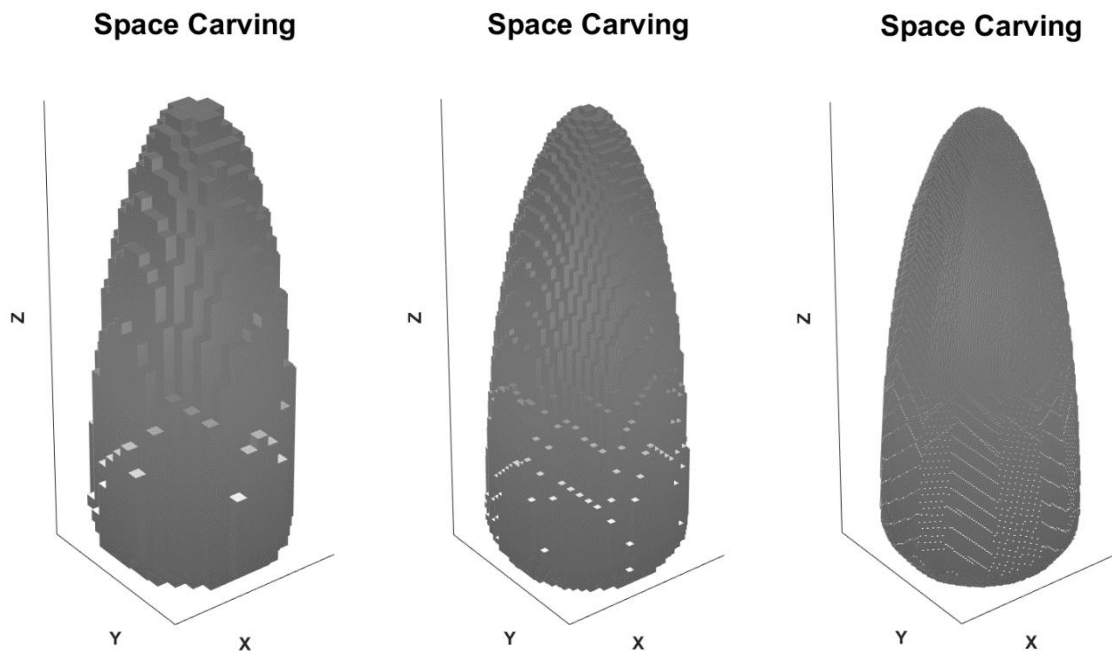


Figure 26 Three resulting space carvings of the flame model at increasing resolution from left to right. The left carving has a resolution of 20x20x40 voxels, the middle 40x40x80 voxels and the right 160x160x320 voxels.

The resulting 3D space carvings (Figure 26) shows a clear visualization of the flame shape, thus indicating that the projection geometry of eight cameras together with a projection image resolution of 960-by-540 pixels is sufficient to capture the outer structure of the flame. Even at the lower resolution of 20x20x40 voxels, the general shape is captured thus leading to the conclusion that this projection geometry should be sufficient for the tomographic technique.

It is of interest to note that this technique requires no large matrixes to be stored except the voxel grid itself. Therefore, less memory storage was needed than in the tomographic reconstruction method thus providing the possibility to utilize a higher voxel resolution without any need for storage optimization.

Tomography

The tomographic reconstruction was performed using ART together with the same eight projection views used for the previous space carving technique. The resolution of the projection images was set to 480-by-270 pixels and an iteration number k of ten together with a relaxation parameter λ set to 0.001 were applied. The resulting 3D tomographic reconstruction had a final spatial resolution of 10x10x20 voxels and can be seen in Figure 27, the low resolution was due to variable storage limitations in the coding structure. The intensity of the reconstruction is scaled between 0 up to 0.13 and a few iso-surfaces are show in Figure 27 at increasing intensity values using the Matlab function *isosurface* [43] to allow the tomographic properties of the reconstruction to be showcased.

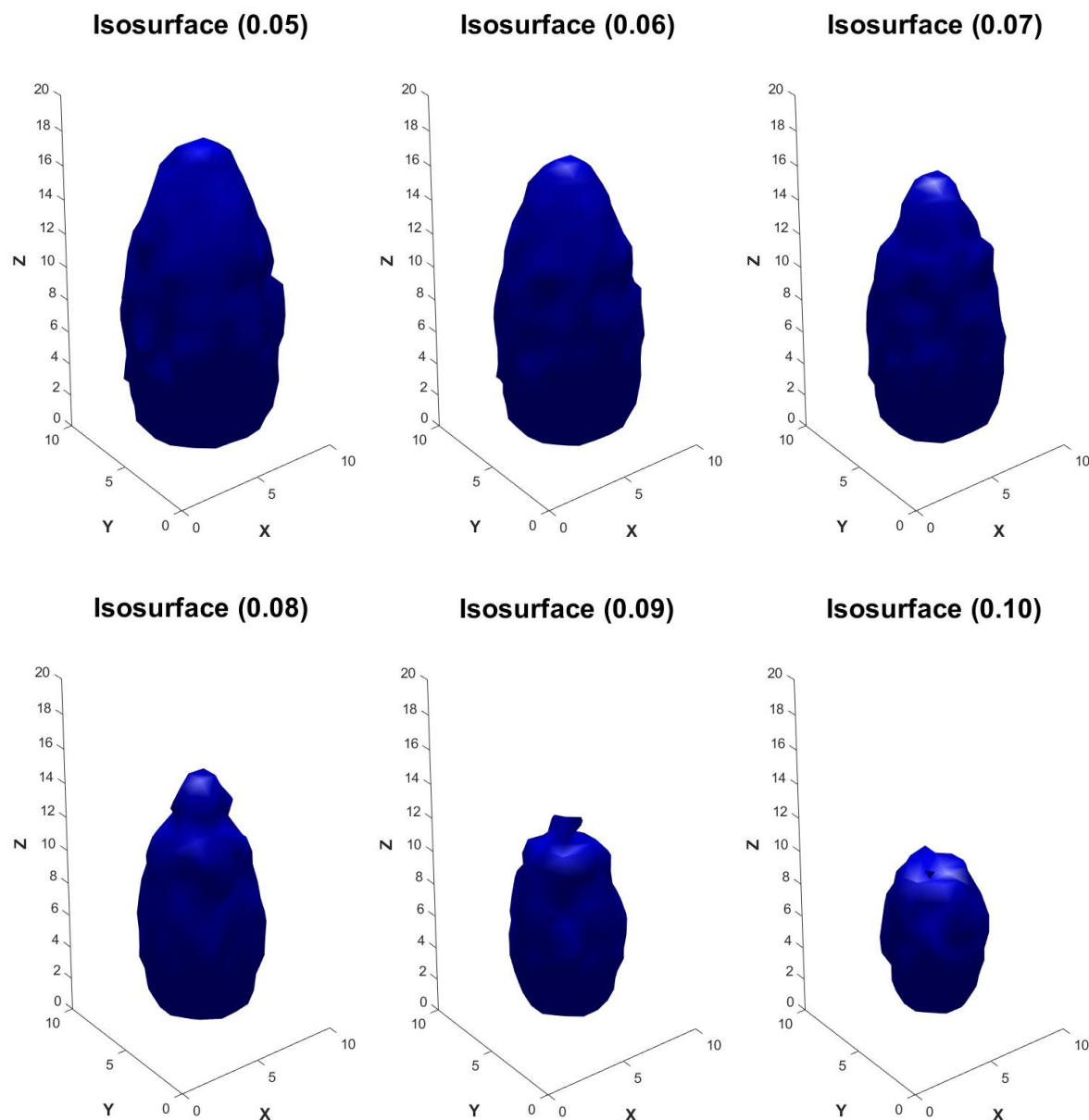


Figure 27 Tomographic reconstruction results. The images are iso-surfaces corresponding to their scaled intensity, starting from the lowest intensity 0.05 at the top left up to the highest at the bottom right 0.10.

The 3D flame model was constructed in such a way that the intensity would be highest in the flame core and gradually decrease further away thus having a non-realistic flame structure without any flame front present. This is verified by the reconstruction (Figure 27) as surfaces corresponding to higher intensity are smaller compared with those of lower intensity and are located closer to the center of the flame.

The general structure of the modeled flame is seen to be captured by the reconstruction, however the rough surfaces are expected to be smoother and the higher intensity surfaces of 0.08-0.09 display distortions at the top of their structure. These aberrations are most likely caused by the utilization of too few voxels which prevents a full visualization of the flame and its features in the given space. Furthermore, the low number of voxels yields few columns in the $[A]$ matrix possible resulting in a more ill-posed equation system to solve and thus less good solution. This problem is most likely removed by reconstruction the flame using a higher voxel resolution together with adding more projection views. However, this could currently not be performed, due to a limitation in the coding structure regarding memory usage, which has to be rewritten.

A vertical slice taken in the middle of the reconstructed volume is shown in Figure 28. The intensity can be seen to steadily increase as the distance to the flame core decreases, this is expected as the 3D flame was created to possess such a structure. However, uncertainties are still present as the surface shapes are rough and uneven at locations through the volume making it hard to accurately determine the locations of specific intensity values.

This result stands as a proof of concept for the 3D tomographic technique applied. Possible future improvements upon this approach would be to modify the data handling and storage in the coding structure to allow for larger projection matrixes $[A]$. This would enable the use of reconstruction spaces discretized into higher voxel resolutions as well as the addition of more projection images with higher resolution. This is expected to allow for better study of limitations and uncertainties for the technique.

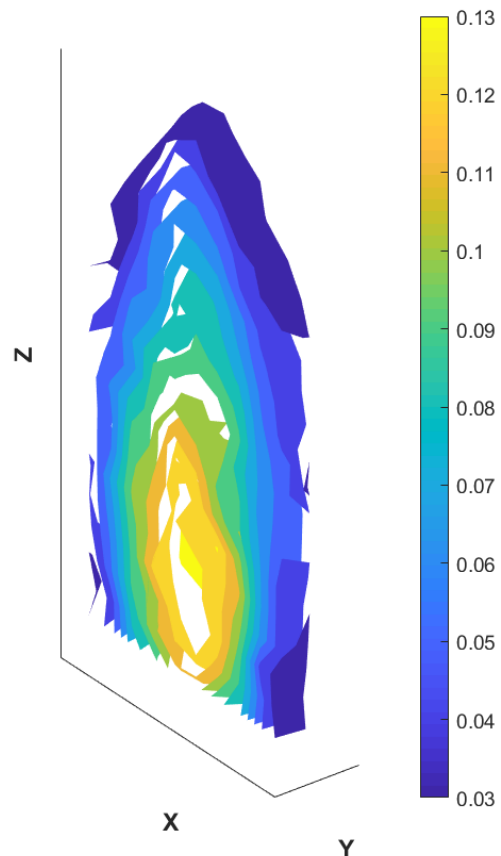


Figure 28 Vertical slice of the tomographic reconstruction. The intensity is observed to increase with a decrease of the distance to the flame core.

Experimental Results

The goal for the construction of an experimental setup and calibrating the camera array of ten cameras was to lay the foundation for a future practical application of the tomographic technique on flames. One requirement for such a setup was to have the ability to image flames with as short exposure time as possible such to freeze the flame movement while at the same time having enough intensity signal to perform a tomographic reconstruction. In Figure 29, two images of the premixed methane flame acquired by one acA1920-40gm-Basler ace camera in the experimental setup are shown. The images were acquired at $3000\mu\text{s}$ and $40\mu\text{s}$, respectively.

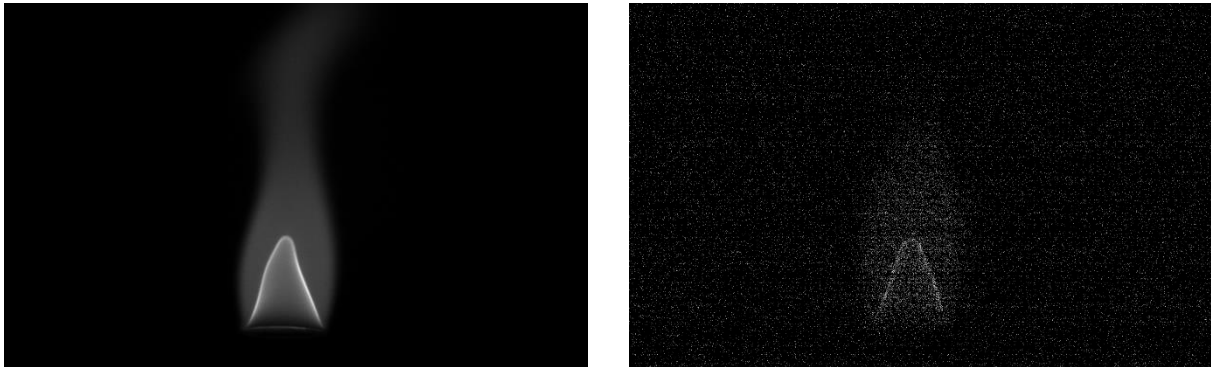


Figure 29 Two images of the premixed methane flame acquired by one of the cameras in the experimental setup. The left image is acquired at an exposure time of $3000\mu\text{s}$ and the right at $40\mu\text{s}$.

This result shows that the signal decreases quite drastically at the shorter exposure time of $40\mu\text{s}$ as expected, nevertheless the signal should be enough to complete a tomographic reconstruction. However, some image post-processing, such as noise removal, on the short exposure time images will be crucial for the implementation of tomographic reconstruction.

The second part was to perform a calibration of the camera array in the setup as outlined earlier. The calibration result for each individual camera was investigated by computing their projection error.

The reprojection error is here defined as the difference between the projected 3D point of a checkerboard corner using the computed camera matrix from the calibration and that same corner point initially detected using feature detection. The position of these two points should ideally be identically placed on the camera image, however if they are not the deviation from each other is given in pixels. This gives a measurement on the accuracy of the computed camera parameter and the resulting camera matrix that projects 3D world coordinates into 2D camera image coordinates. The reprojection result from camera one in the experimental setup can be seen in Figure 30. The results shown are the mean reprojection errors for each individual calibration image acquired by that camera during the calibration process together with the overall mean for all images.

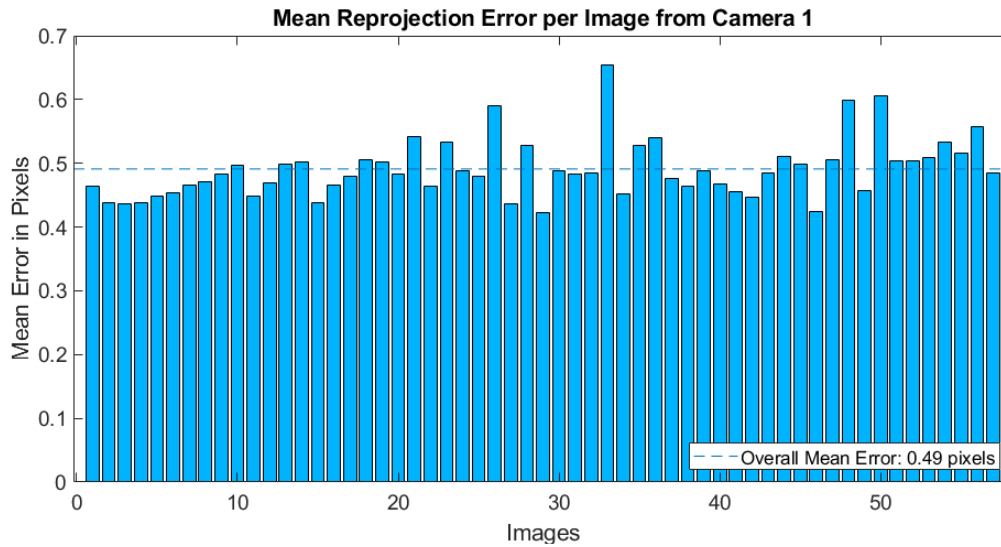


Figure 30 Mean reprojection error for every calibration image from camera one. The overall mean error for this camera calibration was calculated to be 0.49 pixels.

The overall reprojection error for every camera in the experimental setup can be seen in Table 2. The error for each cameras calibration can be seen to be around 0.5 pixels, some slightly below and others above. The small error variance between the cameras is most likely based upon the number of images each camera could use for calibration. Because the calibration target was moved to random positions within the object space of the burner during the calibration process the number of accepted calibration images for each camera did vary. The cameras could not use images where the calibration target was rotated to much or not being completely in the field of view resulting in the inability to detect the corners of the checkerboard boxes. This left each camera with a varying number of calibration images between 55 up to 80 out of the total 90 acquired.

Table 2 Mean reprojection error in pixel values from all ten cameras in the experimental setup, the cameras are identified by their respective numbers.

Overall mean reprojection error in pixels for each camera									
Cam 1	Cam 2	Cam 3	Cam 4	Cam 5	Cam 6	Cam 7	Cam 8	Cam 9	Cam 10
0.49 pixels	0.48 pixels	0.48 pixels	0.48 pixels	0.53 pixels	0.53 pixels	0.53 pixels	0.53 pixels	0.56 pixels	0.54 pixels

All camera locations with respect to each other and the burner were computed by mapping the calibrated cameras to one checkerboard placed at the burner location in such a way that it was clearly visible to all ten cameras. This image then defined the 3D space used to plot the cameras and the result is shown in Figure 31. It should be noted that this way of mapping the cameras using a single flat calibration target needed to be visible for all cameras do not allow for a full 360° camera placement around the target. This does not impact this setup, but it could be of interest for possible future work calibrating cameras for measuring inside combustion devices.

The achieved position results were not completely satisfying and even though approximate camera locations were acquired the necessary accuracy for a tomographic application was not achieved. The result in Figure 31 shows disturbances in many of the calculated camera locations, most notably for camera 9. These disturbances could be related to the fact that a single calibration image was used to map all the cameras into the same coordinate system and thus the quality of that specific image plays an important role when it comes to accuracy. However, one would then expect the positioning of cameras 4,5,6,7, which all have clear frontal views of the calibration target, to show less disturbances than the outer, cameras which is however not the case.

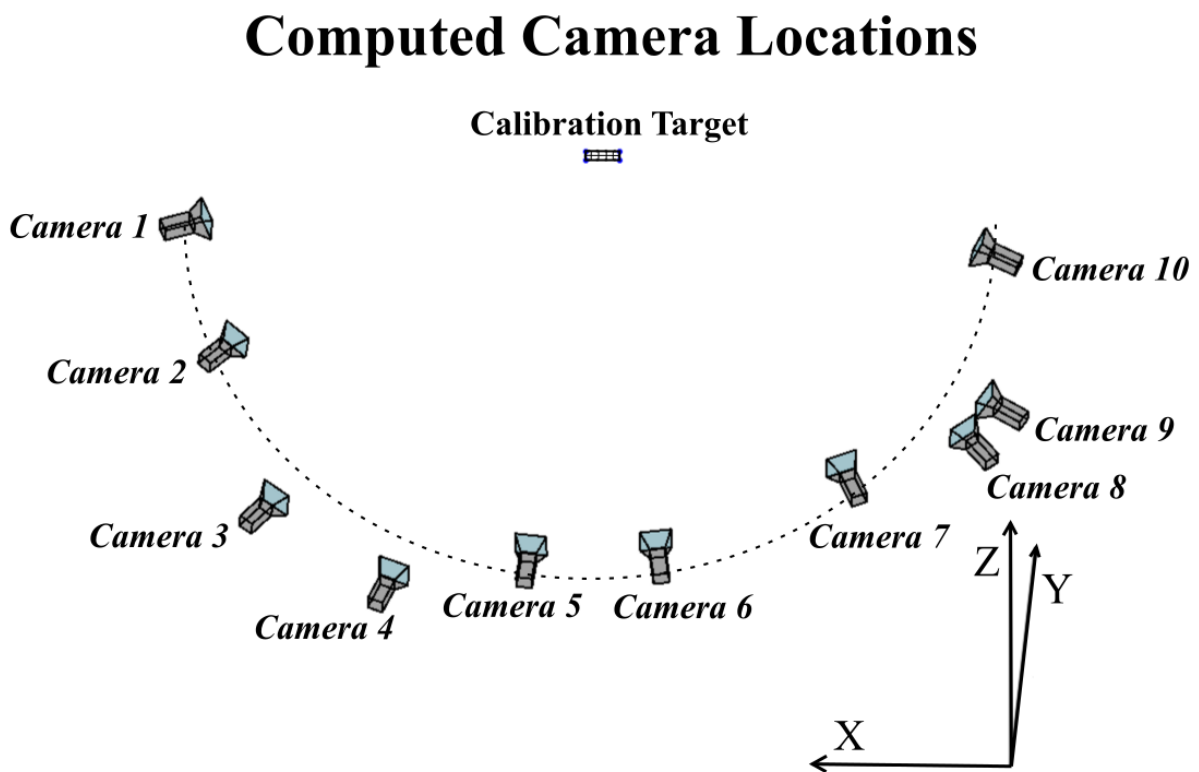


Figure 31 Overview of the calculated camera locations for all ten cameras in the experimental setup as determined by the calibration. The z-direction is the normal of the calibration target, the x-direction is horizontal and the y-direction vertical. The half circle approximates the correct camera placement.

Therefore, it would be of interest in future work to further evaluate this and other calibration techniques to find a suitable result. Techniques that sequentially maps each camera to the previous camera in the array by using multiple calibration images visible by both cameras could be of interest [39]. Likewise, using a 3D-calibration target and allowing simultaneous calibration of multiple cameras at all angles [38], could be viable.

CONCLUSION AND OUTLOOK

The application of ART to solve 2D tomographic reconstruction problems, denoted as a set of linear equations, proved successful in this work. Furthermore, the ability to reconstruct 2D objects of different complexity demonstrated the viability of the employed methods both for acquiring projections of the 2D object and performing the reconstruction. Some expected inaccuracies in the reconstruction results were noticed when the number of projection views of the objects were limited. However, the potential of the technique was clearly shown when ten views were able to quite accurately reconstruct a more complex 200-by-200 pixel flame object.

In the 3D case, the space carving technique were able to accurately acquire the outer-surface of a 3D synthetic flame object at a resolution of 160x160x320 voxels, with even higher resolutions possible. This result proved that the implemented method of utilizing camera matrixes to compute each camera projection image of the 3D object was viable.

The subsequent application of the tomographic technique now expanded to work for 3D objects using 2D projections proved likewise to be successful. Both the shape and internal intensity structure of the imaged synthetic flame object was captured in the reconstruction, with only minor aberrations present. Moreover, the current coding structure puts a limitation on the reconstruction resolution at a maximum of 10x10x20 voxels and future work should focus on the removal of this limit to allow for higher resolutions.

The work towards a laboratory setup to practically apply the tomographic technique was started around ten acA1920-40gm-Basler-ace cameras. This camera model was chosen due to having a superior SNR compared to other models evaluated in this work as well as possessing a high-resolution that could become useful in future work. Ten such cameras were employed in the setup and mapped into a single coordinate system by use of camera calibration. The individual camera calibration results proved satisfactory with a reprojection error of around 0.5 pixels for every individual camera. However, errors in the computed camera locations were present when mapping the cameras together into a single coordinate system, thus providing unsatisfactory results. Improvements upon the camera calibration is therefore of major interest for future continuing work on the experimental setup.

REFERENCES

- [1] Ronald K. Hanson, Jerry M. Seitzman, and Phillip H. Paul, "Planar laser-fluorescence imaging of combustion gases," *Applied Physics B*, vol. 50, pp. 441-454, 1990.
- [2] A. Lozano, B. Yip, and R. K. Hanson, "Planar laser-fluorescence imaging of combustion gases," *Experiments in Fluids*, vol. 13, pp. 369-376, 1992.
- [3] LIN MA, QINGCHUN LEI, TYLER CAPIL, STEPHEN D. HAMMACK, and CAMPBELL D. CARTER, "Direct comparison of two-dimensional and three-dimensional laser-induced fluorescence measurements on highly turbulent flames," *Optics Letters*, vol. 42, pp. 267-270, 2017.
- [4] K. Mohri, S. Görs, J. Schöler, A. Rittler, T. Dreier, C. Schulz, *et al.*, "Instantaneous 3D imaging of highly turbulent flames using computed tomography of chemiluminescence," *Applied Optics*, vol. 56, pp. 7385-7395, 2017/09/10 2017.
- [5] T. D. Upton, D. D. Verhoeven, and D. E. Hudgins, "High-resolution computed tomography of a turbulent reacting flow," *Experiments in Fluids*, vol. 50, pp. 125-134, January 01 2011.
- [6] V. A. Miller, V. A. Troutman, and R. K. Hanson, "Near-kHz 3D tracer-based LIF imaging of a co-flow jet using toluene," *Measurement Science and Technology*, vol. 25, p. 075403, 2014.
- [7] Y. Jin, Y. Song, X. Qu, Z. Li, Y. Ji, and A. He, "Hybrid algorithm for three-dimensional flame chemiluminescence tomography based on imaging overexposure compensation," *Applied Optics*, vol. 55, pp. 5917-5923, 2016/08/01 2016.
- [8] J. Wang, Y. Song, Z.-h. Li, A. Kempf, and A.-z. He, "Multi-directional 3D flame chemiluminescence tomography based on lens imaging," *Optics Letters*, vol. 40, pp. 1231-1234, 2015/04/01 2015.
- [9] Y. Jin, Y. Song, X. Qu, Z. Li, Y. Ji, and A. He, "Three-dimensional dynamic measurements of CH* and C2* concentrations in flame using simultaneous chemiluminescence tomography," *Optics Express*, vol. 25, pp. 4640-4654, 2017/03/06 2017.
- [10] B. R. Halls, J. R. Gord, N. Jiang, M. Splichenko, S. Roy, and T. R. Meyer, "High-speed three-dimensional tomographic measurements for combustion systems," in *32nd AIAA Aerodynamic Measurement Technology and Ground Testing Conference*, ed: American Institute of Aeronautics and Astronautics, 2016.
- [11] Garbor T. Herman, *Fundamentals of Computerized Tomography : Image Reconstruction from Projections*. London New York: Springer, 2009.
- [12] Avinash C. Kak and Malcolm Slaney, *Principles of Computerized Tomographic Imaging*: IEEE Press, 1988.
- [13] Jeremy Floyd, "Computed Tomography of Chemiluminescence: A 3D Time Resolved Sensor for Turbulent Combustion," Doctor of Philosophy, Mechanical Engineering, Imperial College London, 2009.
- [14] J. Floyd, P. Geipel, and A. Kempf, "Computed tomography of chemiluminescence (CTC): instantaneous 3D measurements and phantom studies of a turbulent opposed jet flame," *Combustion and Flame*, vol. 158, pp. 376-391, 2011.
- [15] V. G. Maz'ya and T. O. Shaposhnikova, *Jacques Hadamard: a universal mathematician*: American Mathematical Soc., 1999.
- [16] R. Gordon, R. Bender, and G. T. Herman, "Algebraic reconstruction techniques (ART) for three-dimensional electron microscopy and X-ray photography," *Journal of theoretical Biology*, vol. 29, pp. 471-481, 1970.

- [17] D. A. Forsyth and J. Ponce, *Computer Vision: A Modern Approach*: Prentice Hall Professional Technical Reference, 2002.
- [18] H. Liu, T. Yu, M. Zhang, and W. Cai, "Demonstration of 3D computed tomography of chemiluminescence with a restricted field of view," *Applied Optics*, vol. 56, pp. 7107-7115, 2017/09/01 2017.
- [19] S. Kaczmarz, "Angenaherte auflosung von systemen linearer gleichungen," *Bull. Acad. Polonaise Sci. et Lettres A*, pp. 355–357, 1937.
- [20] W. Cai, X. Li, and L. Ma, "Practical aspects of implementing three-dimensional tomography inversion for volumetric flame imaging," *Applied Optics*, vol. 52, pp. 8106-8116, 2013/11/20 2013.
- [21] R. Hartley and A. Zisserman, "Multiple view geometry in computer vision," *Robotica*, vol. 23, 2005.
- [22] BASLER, "EMVA Data Overview, MONOCHROME AREA SCAN CAMERAS," ed. Germany: BASLER, 2017.
- [23] BASLER, "Basler ace GigE - Product Documentation (User's Manual)," ed. www.baslerweb.com: BASLER, 2018.
- [24] Johnson DH, "Signal-to-noise ratio," *J Scholarpedia*, vol. 1, p. 2088, 2006.
- [25] B. R. Halls, J. R. Gord, P. S. Hsu, S. Roy, and T. R. Meyer, "Development of Two-Color 3D Tomographic VLIF Measurements," in *2018 AIAA Aerospace Sciences Meeting*, ed: American Institute of Aeronautics and Astronautics, 2018.
- [26] Bahaa E. A. Saleh and Malvin Carl Teich, *Fundamentals of Photonics*, 2 ed.: Wiley-Interscience, 2007.
- [27] MathWorks, "MATLAB Function Reference," pp. 8425-8433, 2018.
- [28] Ronald N. Bracewell, *Two-dimensional imaging*. Englewood Cliffs, N.J: Prentice Hall, 1995.
- [29] J. S. Lim, *Two-dimensional signal and image processing*. Englewood Cliffs, NJ: Prentice Hall, 1990.
- [30] MathWorks, "MATLAB Image Processing Toolbox Reference," pp. 2079-2084, 2018.
- [31] P. Christian Hansen and J. Jorgensen, *AIR Tools II: algebraic iterative reconstruction methods, improved implementation*, 2017.
- [32] Blender Documentation Team. (2018, June 29). *Blender 2.79 Manual*. Available: <https://docs.blender.org/manual/en/dev/about/license.html>
- [33] A. W. Fitzgibbon, G. Cross, and A. Zisserman, "Automatic 3D model construction for turn-table sequences," in *European Workshop on 3D Structure from Multiple Images of Large-Scale Environments*, 1998, pp. 155-170.
- [34] K. N. Kutulakos and S. M. Seitz, "A theory of shape by space carving," *International journal of computer vision*, vol. 38, pp. 199-218, 2000.
- [35] MathWorks, "MATLAB Function Reference," pp. 6401-6414, 2018.
- [36] D. Mishra, J. P. Longtin, R. P. Singh, and V. Prasad, "Performance evaluation of iterative tomography algorithms for incomplete projection data," *Applied Optics*, vol. 43, pp. 1522-1532, 2004/03/01 2004.
- [37] J. eM Mikhail and J. Bethel, "McGlone, Introduction to Modern Photogrammetry," ed: John Wiley & Sons, 2001.
- [38] T. Svoboda, D. Martinec, and T. Pajdla, "A convenient multicamera self-calibration for virtual environments," *Presence: Teleoperators & virtual environments*, vol. 14, pp. 407-422, 2005.
- [39] B. Li, L. Heng, K. Koser, and M. Pollefeys, "A multiple-camera system calibration toolbox using a feature descriptor-based calibration pattern," in *Intelligent Robots and Systems (IROS), 2013 IEEE/RSJ International Conference on*, 2013, pp. 1301-1307.

- [40] S. J. Ahn, W. Rauh, and S. I. Kim, "Circular coded target for automation of optical 3D-measurement and camera calibration," *International Journal of Pattern Recognition and Artificial Intelligence*, vol. 15, pp. 905-919, 2001.
- [41] MathWorks, "MATLAB Computer Vision System Toolbox Reference," 2018.
- [42] Z. Zhang, "A flexible new technique for camera calibration," *IEEE Transactions on pattern analysis and machine intelligence*, vol. 22, 2000.
- [43] MathWorks, "MATLAB Function Reference," pp. 6948-6952, 2018.